Electrohydrodynamic conduction phenomena of a viscoelastic dielectric fluid with electroelastic instability

Di-Lin Chen, Yu Zhang, Xue-Lin Gao, Kang Luo, Jian Wu, and Hong-Liang Yi*
School of Energy Science and Engineering, Harbin Institute of Technology, Harbin 150001, People's Republic of China
Key Laboratory of Aerospace Thermophysics, Ministry of Industry and Information Technology, Harbin 150001, People's Republic of China

(Received 8 March 2022; accepted 10 April 2023; published 16 May 2023)

In this paper, we present direct numerical simulations of viscoelastic fluid flow in a cavity with an ion conduction-driven mechanism. The flow patterns, oscillation amplitudes, force competition mode, and power-law spectral scaling accompanying oscillatory flow are examined. The dimensionless parameter β (elucidating the electric-field-enhanced dissociation) together with conduction number C_0 determines the limiting operating regimes (ohmic and saturation). The results demonstrate that asymmetric unsteady flow patterns are observed in perfectly symmetric geometry. Different transition sequences are discussed under two operating regimes, by velocity oscillation and power-law decay. The commensurability magnitudes of the elastic stress and Coulomb forces significantly alter the convective mode, leading to discrepancies in the electroelastic instability paths. The kinetic and elastic energies of the associated driving parameters are quantified, and the flow patterns are divided into five subregions. The dynamic behavior above is related to the strong electroconvective flow within the heterogeneous charge layers.

DOI: 10.1103/PhysRevFluids.8.053702

I. INTRODUCTION

The electrohydrodynamic (EHD) phenomenon, as a multidisciplinary area dealing with the interaction of electric fields and flow fields, has involved many applications, such as multiphase flow [1], flow distribution control [2] (active or passive), heat transfer enhancement [3], spacecraft equipment [4], electronics [5], and robotics [6].

To better reveal the mechanism of the flow motion in dielectric liquids, it is necessary to discuss the origin of the free charges in the flow. Injection, induction, and conduction are the main means of generating a net volumetric charge in dielectric liquids [7]. Charge injection occurs primarily at the electrode-liquid interface, where a neutral electron acceptor molecule can participate in electrochemical reactions to lose electrons. Generally, sharpened electrodes are connected to either the positive or negative terminal of the power supply. Unlike electrical injection, the induction mechanism does not require a charged carrier or additional particles. The discontinuities or gradients in electric conductivity may be the result of an interface between two fluids or a temperature gradient [6,8]. The ion conduction here represents a mechanism in which charged carriers are produced by the dissociation of molecules due to special ionizing admixtures [8–10]. Compared with the former two mechanisms, the ion conduction mechanism has the advantage of not requiring conductivity discontinuities and not deteriorating the fluid properties. When an external electric field is applied, due to the enhanced rate of dissociation over recombination (Onsager-Wien effect),

*Author to whom correspondence should be addressed: yihongliang@hit.edu.cn

the free carriers are adjacent to the electrodes, forming heterocharge layers [called dissociation layers (DSLs)] [11–14]. As a flow phenomenon driven by electrostatic force, the main difference between EHD conduction and electrokinetics (EK) is attributed to the nature of the fluid medium and the generation mechanism of charge carriers. The former mainly occurs in dielectric liquids characterized by low conductivity and permittivity with a dynamic equilibrium between free ions and ionic pairs; however, free ions are naturally present in EK, typically in electrolyte salt solutions. Let us explore the basic scenario of water splitting to show the difference between the two. Many studies [15–19] have reported that, in the study of electroconvective flow (ECF) on an ion-selective membrane surface, water splitting or charge dissociation in membranes will produce more new current carriers, leading to an overlimiting current (OLC). However, in low-conductivity dielectric liquids, water is regarded as a special ionizing admixture (uncontrolled chemical impurity), thus forming some unique ionic cluster structures. Similar admixtures [8] include acetone, butyl alcohol, iodine J_2, oxygen O_2, quinones, sulfur dioxide, and mineral salts. The change in operating regime characteristics is due to the dissolution rate of impurities (or some extra-added specific salts) being much higher than the recombination rate under a specific field strength.

As a promising flow control and heat transfer technique, the fundamental physics of the EHD conduction phenomenon have been rigorously investigated by various researchers over the past few decades. EHD conduction flow on single cylindrical electrodes [20,21], coplanar electrodes [22], three cylinders [23], and two-dimensional planar electrodes [24] has been studied extensively. Feng and Seyed-Yagoobi [25] predicted the characteristic thickness of DSLs, describing the nondimensional field profile and charge density near the electrode. An asymptotic analysis is performed for EHD flow [26], indicating that the EHD flow is dominated by *in vitro* charge-induced flow at large geometric scales and high concentrations. Recently, Vázquez *et al.* [27] developed a mathematical model that can be applied to all sizes (up to micropumps) and discussed in detail the two limiting operating states of EHD conduction pumping: ohmic and saturation. Multiple studies indicate that large electric fields ($>10^6$ V/m) are required for EHD conduction, but this does not limit its wide application, offering practical possibilities for engineering, such as enhanced natural convection [28], solar collectors [29], microscale pumps [30], and coolant control in satellite structural panels [31] with flexible structures [32]. Admittedly, most effective numerical and experimental studies have been performed to investigate pressure generation and heat transfer efficiency in in-out systems [9,10,20–26]. However, a literature review shows that a pure conduction-induced ECF in closed cavities is not available, which is very suitable for studying physical mechanisms and ion transport as well as flow instability [8,24,27].

Many EHD conduction phenomena consider it in terms of Newtonian fluids. However, fluid properties that could serve innovative physical scenarios and engineering applications have not been addressed. Silicone oils, polymer additive solutions, DNA solutions, greases, and coatings exhibit dual characteristics of viscosity and elasticity and are time dependent, called viscoelastic fluids [33]. Additional studies have been performed on microscale electro-osmotic flows (EOFs) with viscoelastic fluids [34–36]. The viscoelasticity formed by surfactants can effectively reduce the frictional drag at high Reynolds numbers [37]. The effects of vertical alternating currents, electric fields, and heat transfer on creeping flow [38] are investigated in dielectric Oldroyd-B fluids. The transition sequences of the thermal instability of a viscoelastic fluid saturated in a porous square cavity were reported [39]. Notably, breakthroughs have been made in studying EHDs with non-Newtonian properties in recent years. The formation of Taylor cone jets in EHD printing [40] has demonstrated the influence of elastic and viscous parameters on the generation of high-resolution patterns. The onset of electroelastic instability [41] in dilute and semidilute polyacrylamide solutions to asymmetric flow over time was observed by visualizing dye patterns. The viscoelasticity also decreases the OLC [34] from convection by up to 40% in the earlier transition from steady to unsteady ECF. The nonlinear behavior of Taylor-Melcher leaky dielectric liquid charged jets has been investigated numerically in one dimension (1D) by the Oldroyd-B model [42]. Recently, our team has also shown the nonlinear behavior of the Oldroyd-B viscoelastic dielectric fluid in EHD unipolar injection, discovering different transition sequences [43,44]. Through a preliminary

literature survey, recent studies on EHD conduction have focused on structural optimization, electrochemical theory, and Newtonian fluid properties [45,46], while complex nonlinear behavior involved has not been discussed.

References [37–44,47] have identified shear thinning, electroelastic instability, transition, and an increase in OLCs induced by viscoelastic fluids. The extension of EHD-related research on complex fluid properties in this paper is motivated by the following aspects. First, the blooming development of aerospace, microelectronics, and medical treatment puts forward requirements for enhanced mixing, microchannel cooling, and mass transfer techniques. The effect of elasticity can cause rapid chaos in the flow field even in a laminar state [33,34,37,41]. Therefore, EHD conduction studies on complex fluid properties may induce flow phenomena and provide ideas for mass, momentum, and heat transport techniques. There are few studies on the EHD conduction mechanism of viscoelastic fluids due to the complexity of the physical model and coupling implementation. Second, in many engineering applications (pipeline transportation, soft robot, etc.), there are defects of large friction impedance and insufficient driving force [8,9]. EHD technology can provide enough power and is very suitable for the improvement of low Reynolds number flow or inefficient pumping. The relevant Newtonian experiments are too numerous [1,3,4,6,8–11] to mention. In contrast, there has been a lack of studies of the effect of viscoelasticity on electroelastic instability. Furthermore, the physical mechanisms, transition sequence, and flow distribution of viscoelastic dielectric fluids are important innovations in Earth and space involving energy transformation, electrochemistry, and biomechanical processes. Consequently, it is necessary to research the complex fluid properties of the EHD conduction mechanism.

We investigate the mechanism of EHD conduction driving for non-Newtonian dielectric fluids described by the Oldroyd-B model with elastic effects. The transition sequence from steady-state, inertia-dominated EHD chaos to elasticity-dominated chaos is observed in our direct numerical simulation (DNS). The dynamic evolution, which has not been addressed in the previous literature, is characterized by oscillation amplitude, kinetic energy and elastic energy, and power-law spectral scaling. We then elucidate the physical mechanisms involved. The remainder of the paper is organized as follows. In Sec. II, we describe an EHD model governing the conduction mechanism of viscoelastic dielectric fluids, and in Sec. III, we briefly describe the benchmark validation. The numerical results are presented and discussed in Sec. IV. Finally, in Sec. V, we summarize the conclusions.

II. PROBLEM FORMULATION

The fluid circulation within a square cavity is investigated, as shown in Fig. 1. The system consists of an enclosure housing with two parallel planar electrodes, and the length of the cathode is equal to the wall. The length of the anode is set to half the width of the cavity and is placed on the left side. The domain is filled with dielectric liquid of density ρ_m, relative permittivity ε_r, and a potential difference $\Delta\phi = \phi_1 - \phi_0$ between the two electrodes. For this asymmetric electrode configuration, with different thicknesses of the DSLs, the electric field forces drive the liquid into motion as expected. The monitoring point M is located at $(0.1d, 0.5H)$ coordinates, where H represents the height of the cavity.

A. Hydrodynamic and electric equations

The incompressible hydrodynamic equations [27] are the momentum equation and the continuity equation:

$$\rho_m\left(\frac{\partial \mathbf{u}}{\partial t} + \mathbf{u}\cdot\nabla\mathbf{u}\right) = -\nabla p + 2\eta_s\nabla\cdot\mathbf{D} + \nabla\cdot\boldsymbol{\tau} + \rho_E\mathbf{E}, \tag{1}$$

$$\nabla\cdot\mathbf{u} = 0, \tag{2}$$

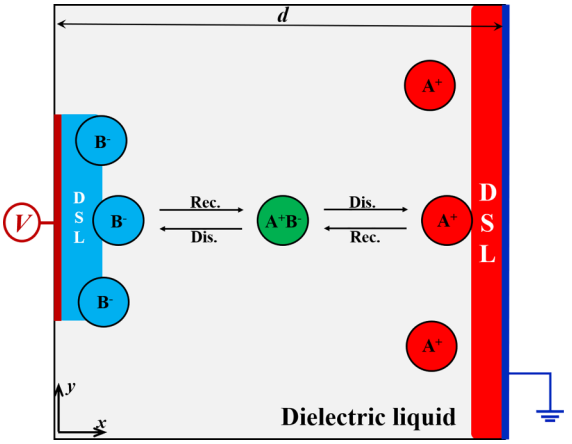

FIG. 1. Schematic diagram of electrohydrodynamic transport between two electrode plates in a cavity. The distance between the two electrodes is characterized as d.

where $\mathbf{u}$ is the fluid velocity, p is the pressure, $\rho_E = e_0(z_+c_+ + z_-c_-)$ is the space charge density, and e is the elementary charge. Here, $z_\pm$ and $c_\pm$ are the valence and concentration of ionic species, respectively. The other parameters are η_s the solvent dynamic viscosity, $\mathbf{D} = \frac{1}{2}[\nabla\mathbf{u} + (\nabla\mathbf{u})^T]$ the ratio of the deformation tensor, and $\boldsymbol{\tau}$ the non-Newtonian polymeric stress tensor, which can be described by different constitutive models.

The electric field and Poisson equations:

$$\mathbf{E} = -\nabla\phi, \tag{3}$$

$$\nabla \cdot (\varepsilon\nabla\phi) = -\rho_E, \tag{4}$$

where ϕ is the voltage, $\mathbf{E}$ is the electric field, $\varepsilon = \varepsilon_r\varepsilon_0$ is the fluid permittivity, and ε_0 is the vacuum permittivity.

B. Dissociation-recombination and ion transport

The chemical dissociation-recombination of neutral species is considered within the electrolyte bulk, considering the fixed neutral species concentration c_0. The reactions of dissociation and recombination are described [27] as

$$AB \underset{\text{rec}}{\overset{\text{dis}}{\rightleftarrows}} A^+ + B^-, \tag{5}$$

where AB is a simple neutral electrolyte species, while A^+ and B^- are the positive and negative ions into which it dissociates. The bulk of the liquid in equilibrium is electroneutral, but near a surface, this balance is disrupted due to the presence of the interface. Consequently, near a surface, an electric double layer (EDL) develops. However, the charge distribution in the EDL is a result of the equilibrium between charge diffusion and ion recombination. If the applied electric field exceeds a certain value, this equilibrium of the surface is broken. Then the Debye layers [8,27,32] are not visible in EDLs, and DSLs develop, forming a charged layer with a thickness λ_H opposite to the electrode polarity. The thickness of the DSLs can be estimated as follows:

$$\lambda_H \approx \frac{\varepsilon K E_0}{\sigma}, \tag{6}$$

where K is the ionic mobility, ε is the fluid permittivity, and σ is the conductivity. Here, E_0 is the order of magnitude of the component of the electric field perpendicular to the surface.

The intensity of the applied electric field does not produce ion injection in any electrodes. Under equilibrium conditions ($c_+^{\rm eq} = c_-^{\rm eq} = c^{\rm eq}$), a reversible reaction can be given as

$$k_{\rm D} c_0 = k_{\rm R} c_+^{\rm eq} c_-^{\rm eq} = k_{\rm R} (c^{\rm eq})^2, \tag{7}$$

where $c_+^{\rm eq}$ and $c_-^{\rm eq}$ are the concentrations of the positive and negative species in equilibrium, respectively. Here, $k_{\rm D}$ and $k_{\rm R}$ represent the dissociation rate and recombination rate, respectively.

When an external electric field $\mathbf{E}$ is applied, the dissociation rate in the DSLs increases significantly more than the recombination with increasing field intensity. This is the electric-field-enhanced dissociation (Onsager-Wien) effect [20]:

$$k_{\rm D}(|\mathbf{E}|) = k_{\rm D}^0 F(b), \tag{8}$$

where $k_{\rm D}^0$ refers to the dissociation rate at thermodynamic equilibrium in the absence of an electric field. Here, $F(b) = I_1(4b)/2b$ is the Onsager function, and b is the enhanced dissociation rate factor. Also, I_1 is the modified Bessel function of the first kind and order 1. Further, b can be calculated by $b = l{\rm B}/l{\rm o}$, with the Bjerrum distance and the Onsager distance [8,10]:

$$l_{\rm B} = e_0^2/4\pi\varepsilon k_B T, \quad l_{\rm o} = \sqrt{e_0/4\pi\varepsilon|\mathbf{E}|}. \tag{9}$$

The equilibrium concentration of the ionic species in field enhancement can be found in Refs. [21,48]. We shall assume that the two species have the same ionic mobility and diffusion coefficients ($K_+ = K_- = K, D_+ = D_- = D$). In addition, the recombination constant $k_{\rm R} = 2e_0K/\varepsilon$ is determined by Langevin's approximation [8,22] to relate the liquid properties. Then the modified Nernst-Planck equation can be written as

$$\frac{\partial c_\pm}{\partial t} + \nabla\cdot(\mathbf{u}c_\pm + z_\pm c_\pm K\mathbf{E} - D\nabla c_\pm) = \frac{2e_0Kc_0^2}{\varepsilon}\left[F(b) - \frac{c_+c_-}{c_0^2}\right]. \tag{10}$$

The left-hand side terms represent the change rate of ion convection, migration, and diffusion fluxes, while the term on the right-hand side refers to the difference in the rates of ionic dissociation and recombination. In DSLs, the generally selected length scale is λ_H, and we have $\frac{D|\nabla c_\pm|}{z_\pm c_\pm K|\mathbf{E}|} \approx \frac{D/\lambda_H}{KE_0} = \frac{\sigma_0 k_B T}{e_0 K\varepsilon E_0^2} \approx 6\times10^{-3}$ (corresponding parameters $\sigma_0 = 2.96\times10^{-8}$ S/m, $K = 2.81\times10^{-9}$ m^2/(sV), $\varepsilon_r = 4.792$, $T = 300$ K, and $E_0 = 10^6$ V/m). Furthermore, in the electroneutral bulk, the diffusion current can be safely ignored even at the microscale due to the relation $\frac{D|\nabla c_\pm|}{z_\pm c_\pm K|\mathbf{E}|} \approx \frac{D/d}{KE_0} = \frac{k_BT/e_0}{E_0 d} = \frac{\phi_T}{\phi_0} \ll 1$. The thermoelectric voltage ϕ_T is ~20 mV at room temperature, and generally, E_0 is $>10^6$ V/m in EHD scenarios [27]. In addition, the assumption of neglecting diffusion is like the result reported by Beunis *et al.* [49] that the effect of diffusion is very low at high voltage (higher than thermal voltage ϕ_T) in the geometry-limited region. This proves that ion diffusion and Debye thickness can be safely ignored both inside the DSL and in the electroneutral bulk [8,20].

C. Log-conformation reformulation and Oldroyd-B model

The Oldroyd-B model, considering a liquid with constant viscosity and high elasticity, is the simplest nonlinear viscoelastic model to describe large deformations of dilute polymer solutions [42,50] with infinite stretching of a single molecule. It has been successfully used for mechanism analysis resulting from pure elasticity [51], electroelastic instability [41], ECF [34,35], nonlinear behavior of a charged viscoelastic liquid jet [42], etc. The Oldroyd-B model is appropriate for primary research on the elasticity effects in EHD conduction-driven flow from initial to steady-state evolution. In general, $\boldsymbol{\tau}$ can be written in terms of the conformation $\mathbf{C}$ in Eq. (1) as

$$\boldsymbol{\tau} = \frac{\eta_p}{\lambda}(\mathbf{C} - \mathbf{I}), \tag{11}$$

where η_p denotes the polymer dynamic viscosity, and λ is the relaxation time for the polymer to relax to the equilibrium state after experiencing some disturbance. Then the conformation transport equation is

$$\frac{\partial \mathbf{C}}{\partial t} + \mathbf{u}\cdot\nabla\mathbf{C} - \left(\mathbf{C}\cdot\nabla\mathbf{u}^T + \nabla\mathbf{u}\cdot\mathbf{C}\right) = -\frac{1}{\lambda}(\mathbf{C}-\mathbf{I}). \tag{12}$$

The high Weissenberg number problem [50,51] exists widely in viscoelastic numerical simulations and can be solved by the log-conformation reformulation (LCR) method. A new variable $\boldsymbol{\Psi}$ is introduced, defined as the matrix logarithm of the conformation tensor $\mathbf{C}$:

$$\boldsymbol{\Psi} = \log(\mathbf{C}) = \mathbf{R}^T \log(\boldsymbol{\Lambda})\mathbf{R}, \tag{13}$$

where $\boldsymbol{\Lambda}$ is a diagonal matrix, the diagonal elements of $\boldsymbol{\Lambda}$ are the eigenvalues of $\mathbf{C}$, and $\mathbf{R}$ is an orthogonal matrix composed of the eigenvectors of $\mathbf{C}$. The evolution Eq. (12) of the conformation tensor $\mathbf{C}$ can be rearranged as

$$\frac{\partial \boldsymbol{\Psi}}{\partial t} + \mathbf{u}\cdot\nabla\boldsymbol{\Psi} - (\boldsymbol{\Omega}\cdot\boldsymbol{\Psi} - \boldsymbol{\Psi}\cdot\boldsymbol{\Omega}) - 2\mathbf{B} = -\frac{1}{Wi}\mathbf{R}(I - \boldsymbol{\Lambda}^{-1})\mathbf{R}^T, \tag{14}$$

where $\boldsymbol{\Omega}$ is an antisymmetric matrix, and $\mathbf{B}$ is a symmetric traceless matrix. The conformation tensor can be recovered from the matrix exponential of $\boldsymbol{\Psi}$ as

$$\mathbf{C} = \exp(\boldsymbol{\Psi}). \tag{15}$$

D. Dimensionless governing equations

The above governing equations can be made dimensionless by using the following variables:

$$\begin{gathered} x, y \sim d, \quad c_\pm \sim c_0, \quad E \sim E_0, \quad \phi \sim E_0 d, \\ u \sim KE_0, \quad t \sim d/KE_0, \quad P \sim \rho_m K^2 E_0^2, \end{gathered} \tag{16}$$

where d is the characteristic length of the system, and E_0 is the order of magnitude of the imposed field. The time scale is the transit ionic time [21,22].

The basic dimensionless EHD equations for viscoelastic fluids are expressed as follows:

$$\frac{\partial c_\pm^*}{\partial t^*} + \nabla\cdot[c_\pm^*(\mathbf{u}^* \pm \mathbf{E}^*)] - \alpha\nabla^2 c_\pm^* = 2C_0\{F[b(|\mathbf{E}^*|)] - c_+^* c_-^*\}, \tag{17}$$

$$\nabla^2\phi^* = -C_0(c_+^* - c_-^*), \tag{18}$$

$$\mathbf{E}^* = -\nabla\phi^*, \tag{19}$$

$$\frac{\partial \mathbf{u}^*}{\partial t^*} + \mathbf{u}^*\cdot\nabla\mathbf{u}^* = -\nabla p^* + \frac{\chi}{\mathrm{Re}_E}\nabla^2\mathbf{u}^* + \frac{1-\chi}{Wi\cdot\mathrm{Re}_E}\nabla\cdot\mathbf{C} + C_0M^2(c_+^* - c_-^*)\mathbf{E}^*, \tag{20}$$

$$\nabla\cdot\mathbf{u}^* = 0, \tag{21}$$

$$\frac{\partial \mathbf{C}}{\partial t^*} + \mathbf{u}^*\cdot\nabla\mathbf{C} = \mathbf{C}\cdot\nabla\mathbf{u}^* + \mathbf{C}\cdot(\nabla\mathbf{u}^*)^T - \frac{1}{Wi}\cdot(\mathbf{C}-\mathbf{I}). \tag{22}$$

Above, the relevant dimensionless parameters in these problems are

$$\begin{gathered} C_0 = \frac{ec^{\mathrm{eq},0}d}{\varepsilon E_0}, \quad \alpha = \frac{k_B T}{e_0 E_0 d}, \quad \mathrm{Re}_E = \frac{\rho_m K E_0 d}{\eta_0}, \\ M = \frac{\sqrt{\varepsilon/\rho_m}}{K}, \quad Wi = \frac{\lambda u_0}{d}, \quad \chi = \frac{\eta_s}{\eta_s + \eta_p}. \end{gathered} \tag{23}$$

The conduction number C_0 characterizes a ratio of two typical times, the ion transport time $t_K = d/KE_0$, and the ohmic time $t_\sigma^0 = \varepsilon/\sigma_0$, and it is a key parameter to differentiate the two

limiting regimes in the EHD conduction phenomenon [24,27]. The diffusion number α is the ratio of the thermal electric field ($E_T = k_B T/e_0 d$) to the imposed electric field (E_0), implying the charge diffusion intensity. The electric Reynolds number Re_E represents the ratio between the Coulomb force (CF) and the viscous force, which is derived using the ion velocity ($u = KE_0$). Here, M is the ratio of hydrodynamic mobility to ionic mobility. The Weissenberg number Wi is the ratio of relaxation time to system characteristic time, and χ is known as the viscosity ratio between solvent viscosity and total viscosity. Note that Re_E acts as a dimensionless applied electric field and is not a hydrodynamic Reynolds number.

Additionally, the Onsager function with the nondimensional electric field in Eq. (17) can be written as

$$F(b) = \frac{I_1(4b)}{2b}, \quad b(|\mathbf{E}^*|) = O^{1/2}|\mathbf{E}^*|^{1/2}, \tag{24}$$

where I_1 is the modified Bessel function of the first kind and order 1, and the Onsager nondimensional number O is

$$O = \frac{e_0^3 E_0}{16\pi\varepsilon k_B^2 T^2}. \tag{25}$$

Generally, the field strength E_0 corresponding to $O = 1$ (calculated under the condition $\varepsilon_r = 5$ at room temperature) is 9 MV/m. When O is $\gg 1$, field-enhanced dissociation must occur. Obviously, according to the dimensionless number C_0 related to the electric field, a new dimensionless number β [27] can be derived:

$$\beta = (C_0 O)^{1/2} = \left(e_0^3 \sigma_0 d/32\pi\varepsilon^2 K k_B^2 T^2\right)^{1/2}. \tag{26}$$

In this paper, different C_0 and β parameters were obtained by adjusting the electric field strength and the characteristic size. Both C_0 and β can be used to characterize the operating regime characteristics (ohmic and saturation), while β is only related to the size d for a given conductivity, implying the Onsager-Wien effect.

E. Numerical implementation and boundary conditions

Generally, the EDL can be safely ignored at the macroscale but not at the microscale. Recently, Vázquez *et al.* [27] proposed that nonmetallic substrates cannot ignore ion diffusion. The electric field generated by the electrodes is parallel to the upper and lower substrates, and the EDL cannot completely disappear. A dimensionless number $\Gamma = \varsigma/E_0\lambda_D = E_s/E_0$ describes the relationship of the Stern surface field with the external field E_0, where E_s is the field strength of the Stern layer. The electric field boundary condition on the top and bottom substrates is $n \cdot \nabla\phi^* = \Gamma = E_s/E_0 = \varsigma/E_0\lambda_D$, where ς is the zeta potential and λ_D is the Debye length. The parameter Γ has profound implications for the ion conduction mechanism operating at the microscale, facilitating the unification of EHD and EK studies [52]. When $\Gamma \ll 1$, i.e., E_s is much smaller than E_0, the external electric field dominates the charge distribution of the substrates, and the ion conduction mechanism is in operation. At $\Gamma \gg 1$, the electric field within the EDL dominates the charge distribution, and the EOF is in operation. The parameter Γ characterizes the transition from the EOF mechanism to ion EHD conduction. However, the scales in this paper, ranging from millimeters to centimeters, are large relative to the EDL thickness (microns). Therefore, the thickness of the EDL can be safely ignored, and only the thickness of the DSL is considered representative. The top and bottom boundaries are solved by the no-slip and zero-ionic penetration conditions [1,2,5,6,21,23,24], which means that $n \cdot \nabla c_+^* = 0$, $n \cdot \nabla c_-^* = 0$, $\mathbf{u}^* = 0$, $n \cdot \nabla\phi^* = 0$.

In addition, the boundary conditions on each boundary type for the governing Eqs. (17)–(22) are

Positive electrode: $c_+^* = 0$, $n \cdot \nabla c_-^* = 0$, $\phi^* = 1$, $\mathbf{u}^* = 0$, $n \cdot \nabla \mathbf{C} = 0$,

Negative electrode: $c_-^* = 0$, $n \cdot \nabla c_+^* = 0$, $\phi^* = 0$, $\mathbf{u}^* = 0$, $n \cdot \nabla \mathbf{C} = 0$.

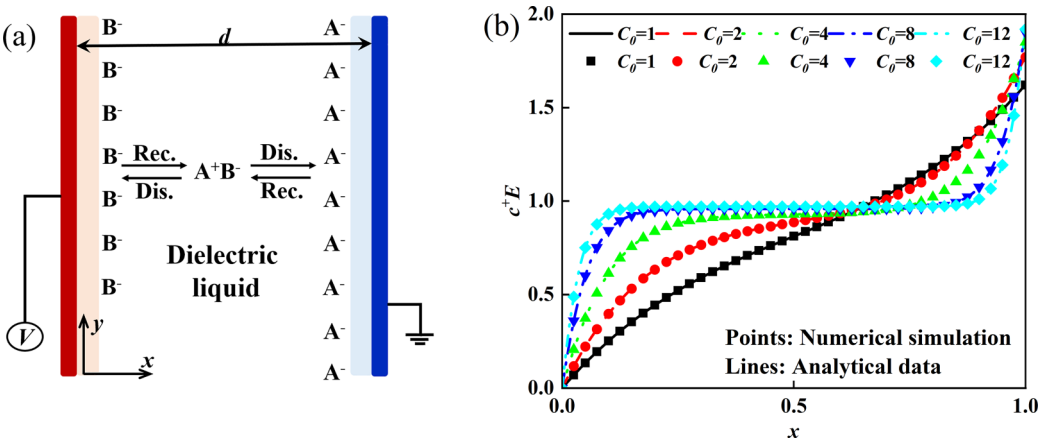

FIG. 2. Comparison of the one-dimensional analytical solution with our present numerical results. (a) Permeable electrodes immersed in dielectric liquid. (b) Profiles of p*E* at various C_0 and $\mathbf{u}^* = 0$.

The set of partial differential equations cannot be solved analytically for most problems due to the complexity and high nonlinearity. In this paper, the numerical study is performed via the finite volume method (FVM) in the open-source OpenFOAM® toolbox, which considers both stability and efficiency. Furthermore, the semi-implicit method for pressure-linked equations-consistent algorithm is utilized to couple velocity and pressure, as the fluid is assumed to be incompressible. All time variables adopt the Euler discrete in the discrete formula, and the gradient term is arranged as a Gaussian linear. The diffusion flux is discretized by the second-order central difference scheme. The convection term of the charge transport equation is discretized by the total variation diminishing scheme [43,44].

The convergent and universally bounded interpolation scheme for the treatment of advection scheme [43] is widely used for the convection term in non-Newtonian problems for the conformation transport equation. In this paper, the LCR method [37,53] is implemented in the solver to automatically guarantee the symmetric positive definite.

III. BENCHMARK VALIDATION

The mathematical model has been obtained in Sec. II. Then the first example is the infinitely long parallel plate structure immersed in dielectric fluid [12], as shown in Fig. 2. The nondimensional governing equations are as follows:

$$d(c_+^*\mathbf{E}^* + c_+^*\mathbf{u}^*)/dx^* = 2C_0(1 - c_+^*c_-^*), \tag{27}$$

$$d(c_-^*\mathbf{E}^* + c_-^*\mathbf{u}^*)/dx^* = 2C_0(1 - c_+^*c_-^*), \tag{28}$$

$$d\mathbf{E}^*/dx^* = C_0(c_+^* - c_-^*), \quad \text{and} \quad \mathbf{E}^* = -d\phi^*/dx^*. \tag{29}$$

The performance of our adopted methodology is satisfactory, with the numerical solution in Fig. 2(b) agreeing well with the analytical solution. In addition, we established the EHD flow around a single wire electrode bounded by a pair of flat-plate electrodes to validate the coupling of ion transport and flow in our previous study [48]. The electrodes are applied with a DC voltage of 1.0 kV, and the central wire electrode is grounded, which is carried out with the experimentally determined zero-field conductivity $\sigma_0 = 2.96 \times 10^{-8}$ S/m and related concentration $c_0 = 5.4 \times 10^{-5}$ mol/m^3. Reference [48] shows a fitted agreement between the velocity trends and the experimental results [21]. The deviation near the symmetry boundary does not exceed 5%. The codes have also been

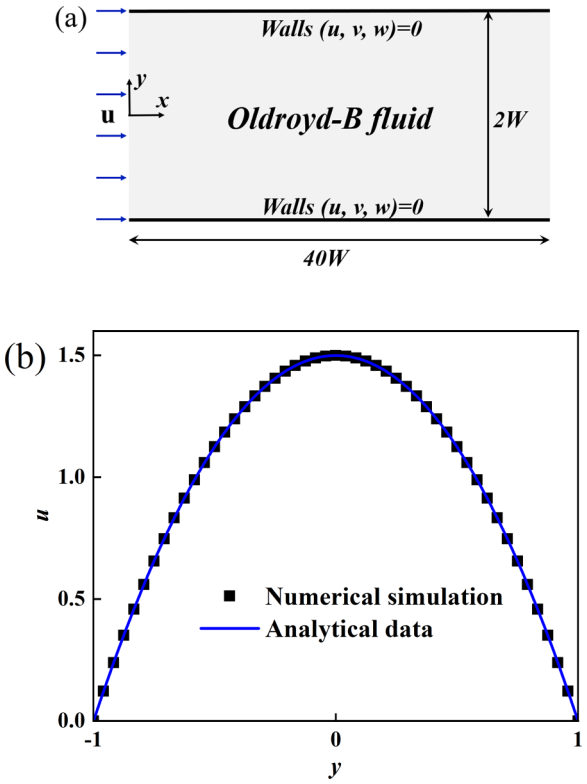

FIG. 3. (a) Sketch of the viscoelastic flow between two infinite parallel plates [54]. (b) The cross-sectional velocity at $x = 35$ for $Re = 0$, $Wi = 0.99$, and $\chi = 0.01$.

validated by lid-driven cavity flow [48] of viscoelastic liquids. Thus, all these results suggest that our codes can accurately simulate the problem considered in this paper.

For the viscoelastic fluid module, the flow between two infinite parallel plates [54] is simulated as a benchmark in Fig. 3. The results of the FVM fit well with the literature draft test in Fig. 3(b). The above results demonstrate the ability of the codes to simulate Oldroyd-B viscoelastic fluid flow and the excellent implementation of the LCR method. Although no experimental or numerical simulations relating to EHD conduction in viscoelastic fluids have been reported, the authenticity and reliability of our DNS is guaranteed by multiple validation benchmarks. Finer meshes are constructed near the electrodes to capture the thin DSLs in Fig. 1. Computation domain meshes have a minimum element size of 10 nm and a maximum growth rate of 1.3. The mesh convergence tests show that accurate numerical results can be obtained when the number of mesh elements is 40 000, 60 000, or even 12 000. The appropriate unit (60 000) was used in this paper to ensure fast convergence.

IV. RESULTS AND DISCUSSION

Most experimental and numerical studies have focused on elastic instabilities in pressure-driven systems. In contrast, little attention has been given to destabilization mechanisms in EHD systems. Therefore, the EHD conduction flow in a viscoelastic dielectric liquid is solved by DNS, investigating the transition sequences and dynamic properties. Moreover, we implement the polymer elasticity for Newtonian fluid $Wi = 0$, weak elasticity $Wi = 0.1$, moderate elasticity $Wi = 0.5$, high elasticity number $Wi = 2$, and even higher. If the polymer polyisobutylene is added into it, the viscosity ratio

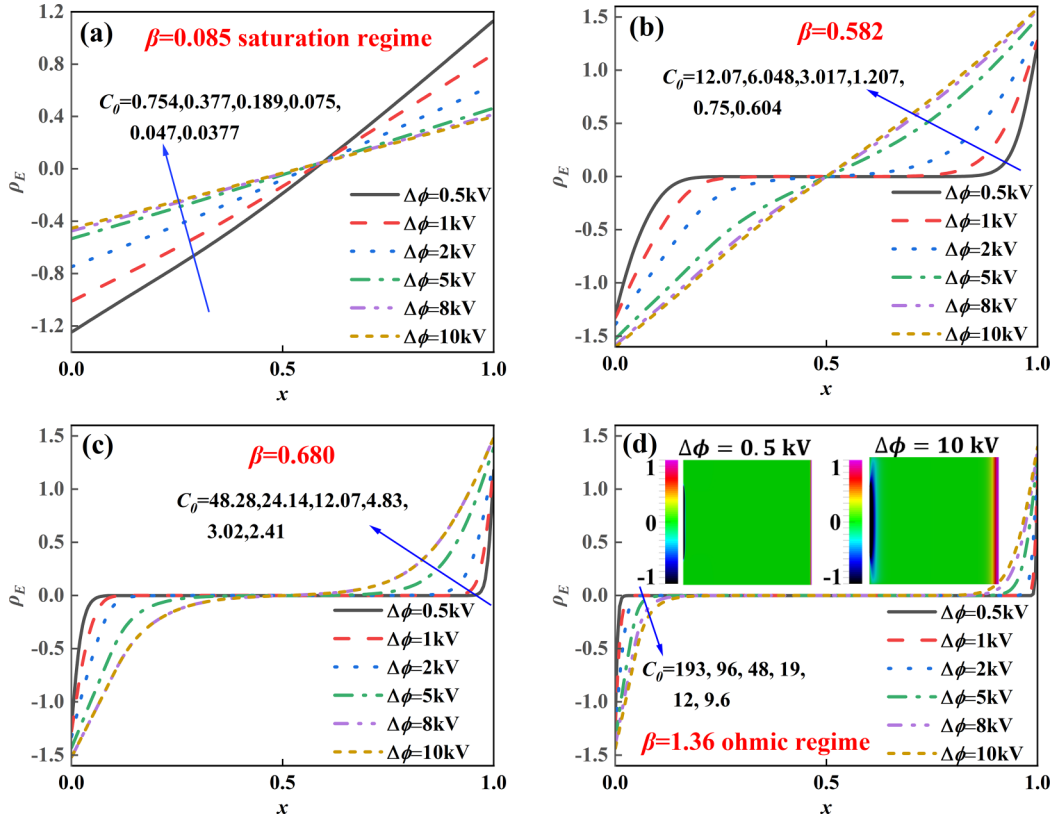

FIG. 4. Net charge density distribution at different β values, the influence of voltage, with a fixed level of conductivity $\sigma_0 = 0.5 \times 10^{-8}$ (S/m).

is kept at $\chi = 0.8$. The working fluid, refrigerant R-123 [24,55], is used to characterize fluid properties for low-conductivity dielectric fluids with experimentally determined zero-field conductivity $\sigma_0 = 0.5 \times 10^{-8}$ S/m, and the other physical parameters are $\varepsilon_r = 4.792$, temperature $T = 300$ K, Newtonian viscosity $\eta_s = 4.087 \times 10^{-4}$ pa s, and $\rho_m = 1452$ kg/m^3. In addition, we obtain the ionic mobility $K = 3.899 \times 10^{-8}$ m^2/(sV) and the diffusion rate $D = 1.0078 \times 10^{-9}$ m^2/s.

Below, we begin with the base characteristics of the EHD conduction phenomenon under different Onsager-Wien effects (β) and conduction numbers (C_0). Second, the electroelastic instability is investigated in detail, including the net charge density distribution, instantaneous velocity evolution, fluctuation amplitude, Fourier spectrum, and power spectral density (PSD). Third, a global assessment of the elastic and kinetic energies of the flow field and force competition mechanisms is presented. Finally, the transition sequences to chaos are given over a wide range of parameters.

A. Field-enhanced dissociation effects for β

Having discussed the effect of the conduction number in our previous study [48], we now turn to the combined effect of the coupling number C_0 and the parameter β with the field-enhanced dissociation effects. According to $\beta = [e_0^3 \sigma_0 d/32\pi\varepsilon^2 K k_B^2 T^2]^{1/2}$, the conductivity is fixed at $\sigma_0 = 0.5 \times 10^{-8}$ (S/m) in the discussion of this section, and the obtained β can range from 0.085 to 1.36 by regulating the difference sizes d, as shown in Fig. 4. In addition, adjustable voltages range from 0.5 to 10 kV to obtain different C_0 values.

TABLE I. Typical selected cases for electroelastic instability with relevant physical properties and important parameters.

Cases	Conductivity (S/m)	Voltage (kV)	d (mm)	Re_E	C_0	β	Operating regime
1	0.5×10^{-8}	1	0.5	110	0.375	0.085	Saturation
2	0.5×10^{-8}	0.5	0.5	50	0.754	0.085	Saturation
3	0.5×10^{-8}	1	2	110	6.05	0.582	Ohmic
4	0.5×10^{-8}	0.5	2	50	12.07	0.582	Ohmic
5	0.5×10^{-8}	1	8	110	96.56	1.36	Ohmic
6	0.5×10^{-8}	0.5	8	50	193	1.36	Ohmic

Figure 4 shows the combined effect of the conduction number C_0 and the parameter β. For a small value of β ($\beta = 0.085$) in Fig. 4, the system operates under the saturation regime in all cases, regardless of the high or low magnitude of the voltage. As β increases (at $\beta = 0.582$), the system may shift in the ohmic and saturation regimes as the voltage changes. Upon further increasing the value of β, the system gradually shifts to a pure ohmic operating regime. When β increases significantly to > 1 ($\beta = 1.36$), the system continuously remains in the ohmic regime. As shown in Fig. 4, different voltages determine the field strength and C_0. In addition, it is worth mentioning that the system can always operate in the ohmic regime without saturation [27] by adjusting the β parameters.

For $\beta = 0.582$, the ohmic regime gradually disappears and is replaced by a saturation regime, while the C_0 value can range from $C_0 > 1$ to $C_0 < 1$ as the voltage increases from 0.5 to 10.0 kV. Several reports [27,48] have noted that $C_0 = 1$ is the critical value for the transition of EHD conduction from the saturation to the ohmic regime. No electroneutral bulk is observed in the $\beta = 0.085$ case. The increase in field strength corresponds to the decrease in C_0, which indicates that the thickness of the DSLs tends to increase and overlap. However, the dissociation of electrolytes is enhanced, and more ions are expected since the Onsager effect is considered in our results. As β increases further to $\beta = 0.680$, it can be expected that the system is maintained in the ohmic regime with more dissociated ions due to the Onsager-Wien effect, where the structures of DSLs and electroneutral bulk may appear. Moreover, for $\beta > 1$, the system operates in the ohmic regime even at very high voltages ($\Delta\phi = 10.0$ kV), where field-enhanced dissociation occurs more strongly. The insets in Fig. 4(d) show the contour maps of the CF $[\rho_E E = e(c^+ - c^-)\phi/d]$ for $\Delta\phi = 0.5$ and 10 kV. The CF gradually decreases along with the electrode plates at both ends toward the centerline, and the CF acts inside the finer DSLs at low voltages. As the voltage increases, the area of influence of the CF increases significantly, and the driving force is enhanced. An additional discussion of C_0 in cavity flow, including net charge density properties as well as vortex distribution, is presented in the Appendix.

The discussion of β parameters in this section dominates the different size and conduction operating regimes, which set the stage for the flow pattern and instability analysis that follows. Therefore, we select several typical settings to research the electroelastic instability in Table I with relevant physical properties and important parameters.

B. Electroelastic instability

This section numerically implements the different electric field-enhanced dissociation numbers β with continuous conduction numbers C_0 (from $C_0 = 0.377$ to 12.07) for viscoelastic fluids. By precisely tuning the Wi parameters, we will analyze the rich structural changes in the flow field and the complex nonlinear dynamics during the transition from steady state to periodic oscillations and finally to chaotic states.

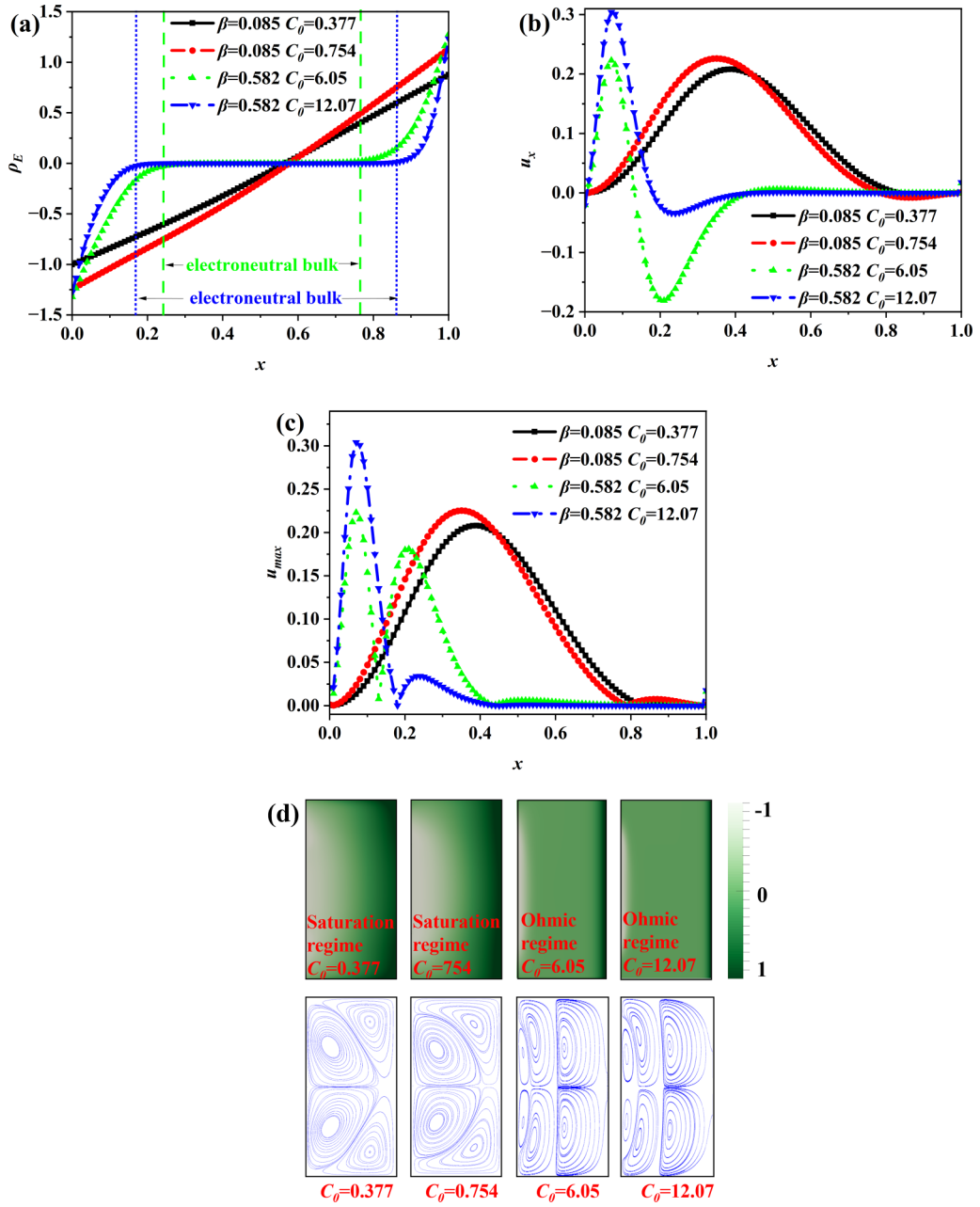

FIG. 5. The net charge density and velocity distribution patterns. (a) Net charge density, (b) x-component velocity, (c) velocity amplitude, and (d) net charge density cloud (top), streamline (bottom). Four cases were selected, including case 1: $\beta = 0.085$, $C_0 = 0.377$; case 2: $\beta = 0.085$, $C_0 = 0.754$; case 3: $\beta = 0.582$, $C_0 = 6.05$; and case 4: $\beta = 0.582$, $C_0 = 12.07$.

As shown in Fig. 5, we give the net charge density characteristics, x component, and amplitude velocity operating in the saturation and ohmic regimes. Figure 5(d), top, shows the net charge density contour plot, and Fig. 5(d), bottom, shows the streamline plot. From left to right, the sequences corresponding to the conduction numbers of $C_0 = 0.377$, 0.754, 6.05, and 12.07, i.e.,

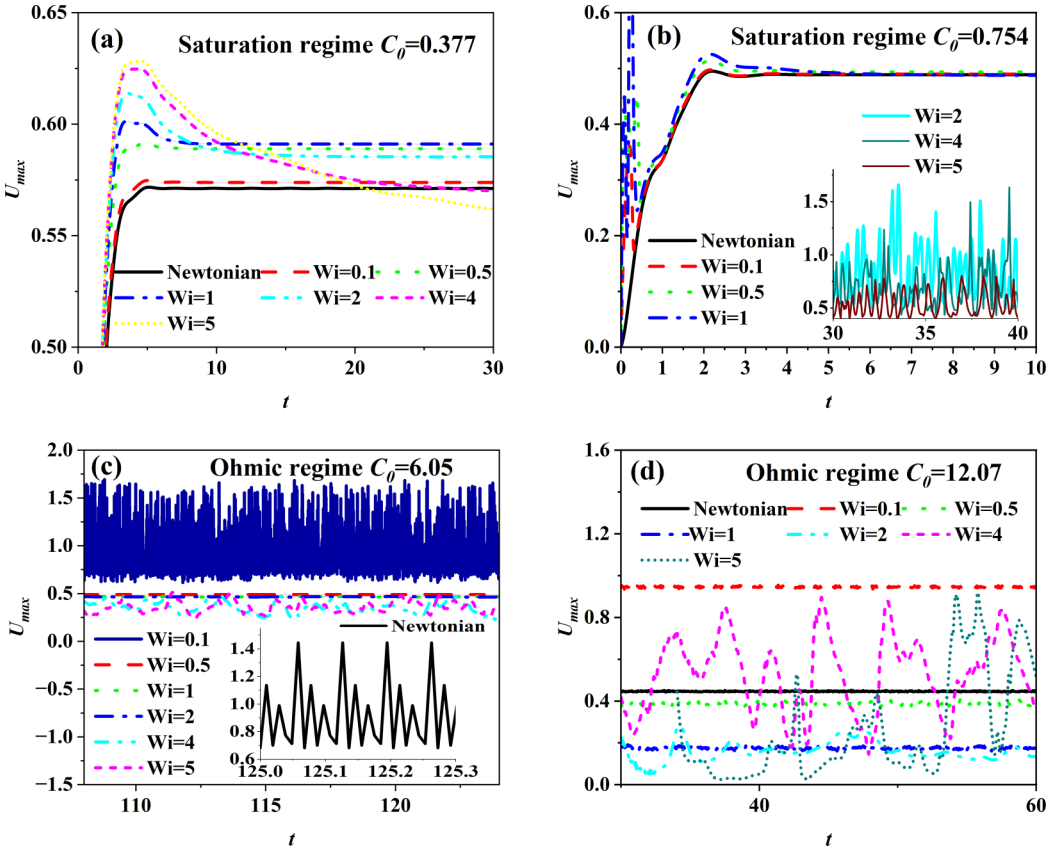

FIG. 6. Evolution of maximum velocity with time. (a) $\beta = 0.085, C_0 = 0.377$; (b) $\beta = 0.085, C_0 = 0.754$; (c) $\beta = 0.582, C_0 = 6.05$; and (d) $\beta = 0.582, C_0 = 12.07$.

the change from the remarkable saturation regime to the ohmic regime, are shown in order. The significant electroneutral bulk indicates the classic ohmic operating regime in Fig. 5(a), and the DSL thickness becomes thicker as C_0 decreases. When decreasing to $C_0 < 1$, the transition to the saturation state is demonstrated as the overlapping feature of DSLs. The above operating regime features can be found in several studies [2,5,12,27], which are unified with the results in Fig. 5 and the Appendix. Figures 5(b) and 5(c) also demonstrate the different velocity distribution features under the two regimes, forming the centrosymmetric four- and six-vortex structures in Fig. 5(d), respectively. Similar vortices are also observed in the numerical solution based on the lattice Boltzmann method [24].

Figure 6 shows the evolution of the maximum velocity with time for different polymer elasticities. Overall, the velocity reaches a maximum at the end of acceleration and then gradually decreases and progresses to a steady state, as shown in Figs. 6(a) and 6(b). The higher the elasticity of the polymer, the longer the evolution time to the steady state, which is consistent with some relevant findings for microchannel flow of viscoelastic fluids [51,56]. In the range of parameters studied in the strong saturation regime ($C_0 = 0.377$), no electroelastic instability occurs with a constant velocity at steady state. In contrast, the effect of elasticity on the maximum velocity of the flow field is significant in Figs. 6(c) and 6(d), as the flow field characteristics in the weak saturation or ohmic regimes are established. To draw a conclusion, an increase in Wi numbers leads to an increase in $U_{\max}$ when operating in the saturation regime. At $C_0 = 0.754$, the $U_{\max}$ increase at $Wi \leqslant 2$ is the result of the energy release into the flow field by the compression of polymer molecules. At

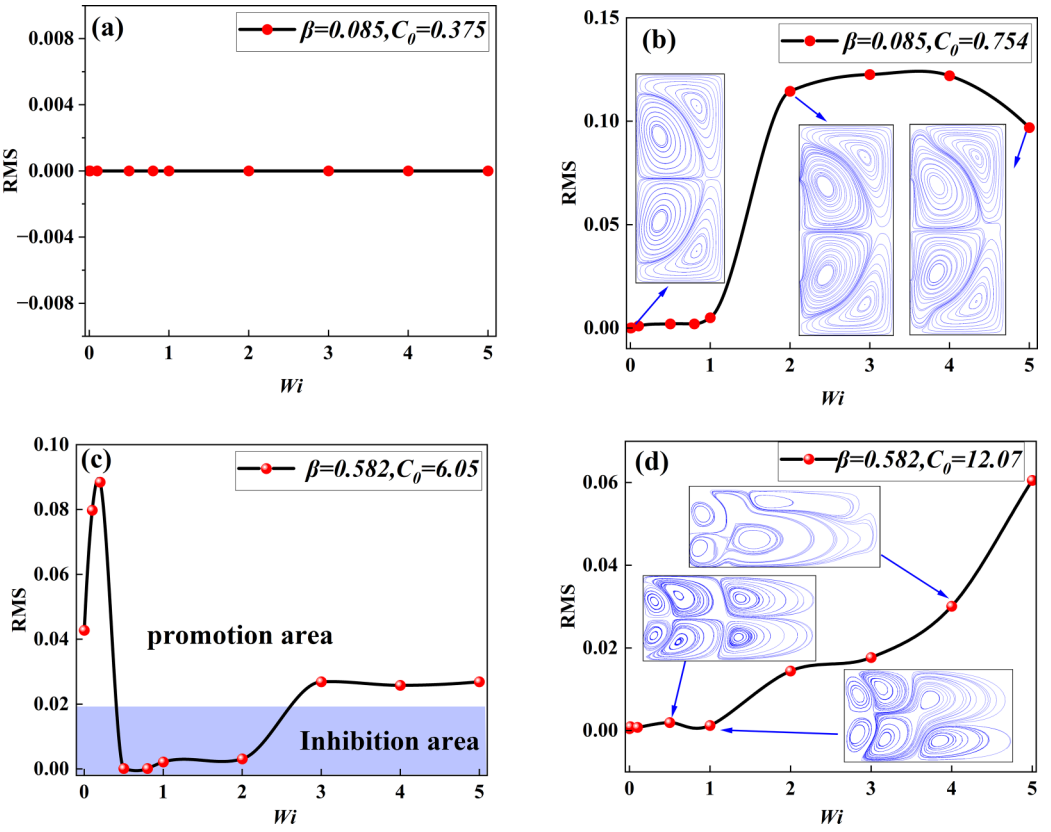

FIG. 7. Root mean square (RMS) of the velocity fluctuation at monitoring point M. (a) $\beta = 0.085$, $C_0 = 0.377$; (b) $\beta = 0.085$, $C_0 = 0.754$; (c) $\beta = 0.582$, $C_0 = 6.05$; and (d) $\beta = 0.582$, $C_0 = 12.07$.

higher Wi numbers, however, $U_{\max}$ decreases, but the pulsation frequency intensifies. This may be due to the increase in elastic elements in the flow field and the energy conversion effect, where more kinetic energy is converted to elastic energy to be stored by the polymer molecule (like a bead-spring structure) units [48]. Under the ohmic regime in Figs. 6(c) and 6(d), a different profile from that of the saturation regime is shown. As the polymer elasticity increases, $U_{\max}$ shows a tendency to increase and then decrease. This may be a result of the occasional burst element of elasticity and symmetry breaking [51,57] of the flow field. At smaller Wi numbers, the polymer molecules are mostly compressed in the steady state, releasing energy into the flow field. However, at large Wi numbers, the molecular stretching effect is dramatic, and the polymer molecules absorb more kinetic energy from the main flow, resulting in a decrease in $U_{\max}$.

The fluctuated velocity represents the time-dependent discrepancy from the time-averaged value, represented by the root mean square (RMS) [48]. There are no instability fluctuations in the range (from $Wi = 0$ to 5) of $C_0 = 0.377$, i.e., the CF dominates the flow behavior for a field strength of O (10^7 V/m) in the strong saturation regime, as shown in Fig. 7(a). As the system enters a weak saturation regime ($C_0 = 0.754$), the RMS fluctuations are evident at $Wi = 2$. The Wi number changes the flow pattern characteristics in the RMS of the inset in Fig. 7(b), which manifests as vortex expansion near the positive plate and vortex compression near the negative plate. This can be explained by the fact that, as the Wi number increases, the stresses are concentrated near the four corners of the computational domain, forcing the flow field into compression near the four corners. In addition, Fig. 8 shows the results of the statistical averaging of the first normal stress difference

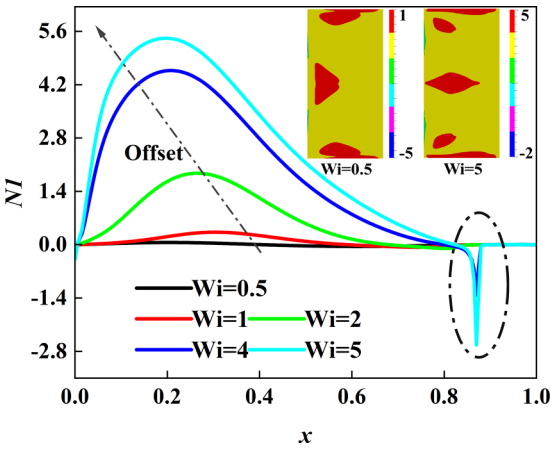

FIG. 8. The first normal stress difference under different Wi values, taking the value along $y = 0.5$. The inset shows the cloud maps for $N1$, $Wi = 0.5$ (left), $Wi = 5$ (right).

($N1 = \tau_{yy} - \tau_{xx}$) along the central line of the positive and negative plates. Several studies have shown that $N1$ is crucial in the flow transition and distribution in viscoelastic fluid flow [33,48]. The amplitude of $N1$ appears to show a shift toward the vicinity of the positive plate as the Wi number increases. In contrast, the influence of the elastic force (EF) is mainly reflected in the stretching and distortion of the vortex near the negative plate due to having a lower ion-driven flow rate relative to the positive plate. In the insets of the $N1$ contour in Fig. 8, the region of stretch-shear stress gradually deforms as Wi increases, moving toward the center near the positive plate and squeezing toward the negative plate and the walls. The above results provide further evidence that the instability of the viscoelastic fluid originates at the four corners of the DSLs and that the high shear strain rate inside the DSL plays a key role. Therefore, in Fig. 7(c), the velocity RMS increases first, then decreases, and then increases with increasing Wi number. We attribute the second RMS increase to the release of elastic energy of polymer molecules in the flow field dominated by elastic instability. Elastic-dominated instability flow will cause a typical symmetry-breaking phenomenon [57], such as the vortex diagram shown in Fig. 9. Moreover, after our arguments, the above results are equipped with time-dependent asymmetric flow and are not like the steady asymmetric flow in pressure-driven systems [33,58,59]. Figure 7(d) shows the RMS in the high conduction number $C_0 = 12.07$. At $Wi = 0.5$, the vortex still shows clear symmetry with a weak oscillatory state. When the Wi number increases further ($Wi = 4$), symmetry is completely lost, and the flow field enters elastic instability. Overall, we attribute the characteristics of velocity fluctuation at low Wi numbers to the fact that the effect of elastic stress is much lower than that of CF, and inertia-dominated EC fluctuations (no symmetry breaking) develop. The characteristics of velocity fluctuation in the case of high $Wi > 2$ are attributed to elastic instability, accompanied by symmetry breaking. The above results are identified and analyzed by the power spectrum next. In addition, the contribution analysis below of the convection term, CF, and elastic stress also shows that the above results are mainly caused by the competitive mechanism of the CF and elastic stress in the momentum equation.

One way to observe the flow state is to calculate the PSD of the time series. Then the exponent of the power-law decay $P \propto f^{-n}$ with frequency f is measured after the chaotic flow is developed. Generally, 600–1200 time steps are selected in some postprocessing processes, and the results under the whole time series are compared. We have also computed the power spectra without part of the time series, and the results are similar. It is known from Fig. 7(a) that the system is ultimately steady state for several Wi conditions. Therefore, the corresponding frequency spectral features in the strong saturation regime $C_0 = 0.377$ are not given here.

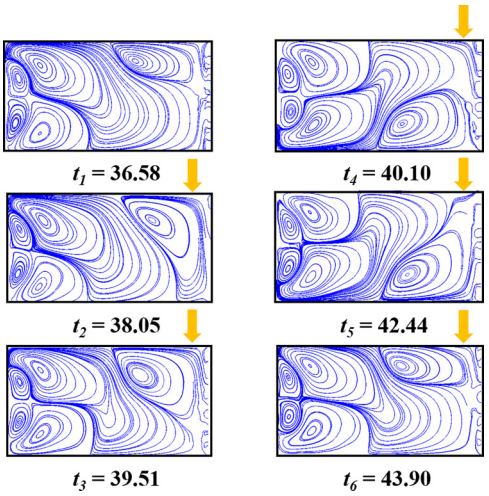

FIG. 9. The asymmetric oscillatory flow characteristics for $Wi = 2$. Similar flow patterns and vortex distributions are shown in t_1 and t_6.

In Fig. 10(a), the log-log plot of the PSD of the weak saturation regime $C_0 = 0.754$ shows that white noise is observed for all conditions with $Wi \leqslant 1$. According to an asymptotic negative power law, the experimental study of Malraison and Atten [60] has shown that the PSD obeys an exponent $n = 7 \pm 1$ decay in the high frequency of the inertially dominated regime. As shown in Fig. 10(a), we obtain $n = 6.8$ at the $Wi = 5$ condition, which is consistent with the exponential ranges found in experiment by Malraison and Atten [60]. For the viscoelastic fluid with $Wi = 4$, the exponent $n = 6.1$. When Wi is decreased to 3 and 2, the corresponding values are 4.2 and 4.1, respectively. Although the different exponents found here suggest that elasticity may modify the statistical properties of the velocity fluctuations, the deviation from the lower bound of a value obtained in the experiment is slight. Because the value of Re_E corresponding to the inertial regime is relatively lower, the term $\frac{1-\chi}{Wi \cdot \mathrm{Re}_E} \nabla \cdot \mathbf{C}$ on the Navier-Stokes equation [Eq. (20)] is divided by Re_E, making it a matched role in strength compared with the Coulomb term $C_0 M^2 (c_+^* - c_-^*) E$. Therefore, the decay exponents n corresponding to various Weissenberg numbers are very different from the Newtonian fluid. In other words, as the polymer elasticity increases in our cases, the system transitions from steady-state flow to an inertia-dominated power-law decay of EHD instability, obeying $n = 6.8$. That is, in our results, the path from steady-state transition to inertia-dominated EHD chaos is observed in a weak saturation regime.

When the system enters the ohmic regime, the inset of Fig. 6(c) shows a fully developed steady periodic self-excited oscillation with Newtonian fluid. The main peak $f_1 = 28.588$ in the Fourier spectrum shows the fundamental frequency of this self-excited periodic oscillation in Fig. 10(b), and the rest of the secondary peaks are multiples of the harmonics of the main peak, indicating that the flow is in a single-cycle oscillation mode. When $Wi = 0.1$, the flow becomes a quasiperiodic oscillation with multiple incommensurable frequencies. At $Wi = 0.5$ and 0.8, the system enters steady flow. The number of Wi continues to increase to 2, at which the Fourier spectrum of the time series of velocity fluctuations takes the form of a continuous broadband characteristic, and the system exhibits typical chaotic convection. However, the Fourier spectra with distinct single-peak frequencies $f_1 = 50.40$ and $f_2 = 78.2$ can still be observed at $Wi = 2$, as shown in Fig. 10(b). This phenomenon is because of both chaotic and periodic oscillatory features presented in the flow. The prominent single-peak frequencies indicate that the system maintains regularity and correlation, while the spectral broadband is the concrete manifestation of the chaotic element in the flow. At $Wi = 3$, the PSD exhibits a power-law decay of $n = 6.5$ in the mid/high-frequency range, consistent

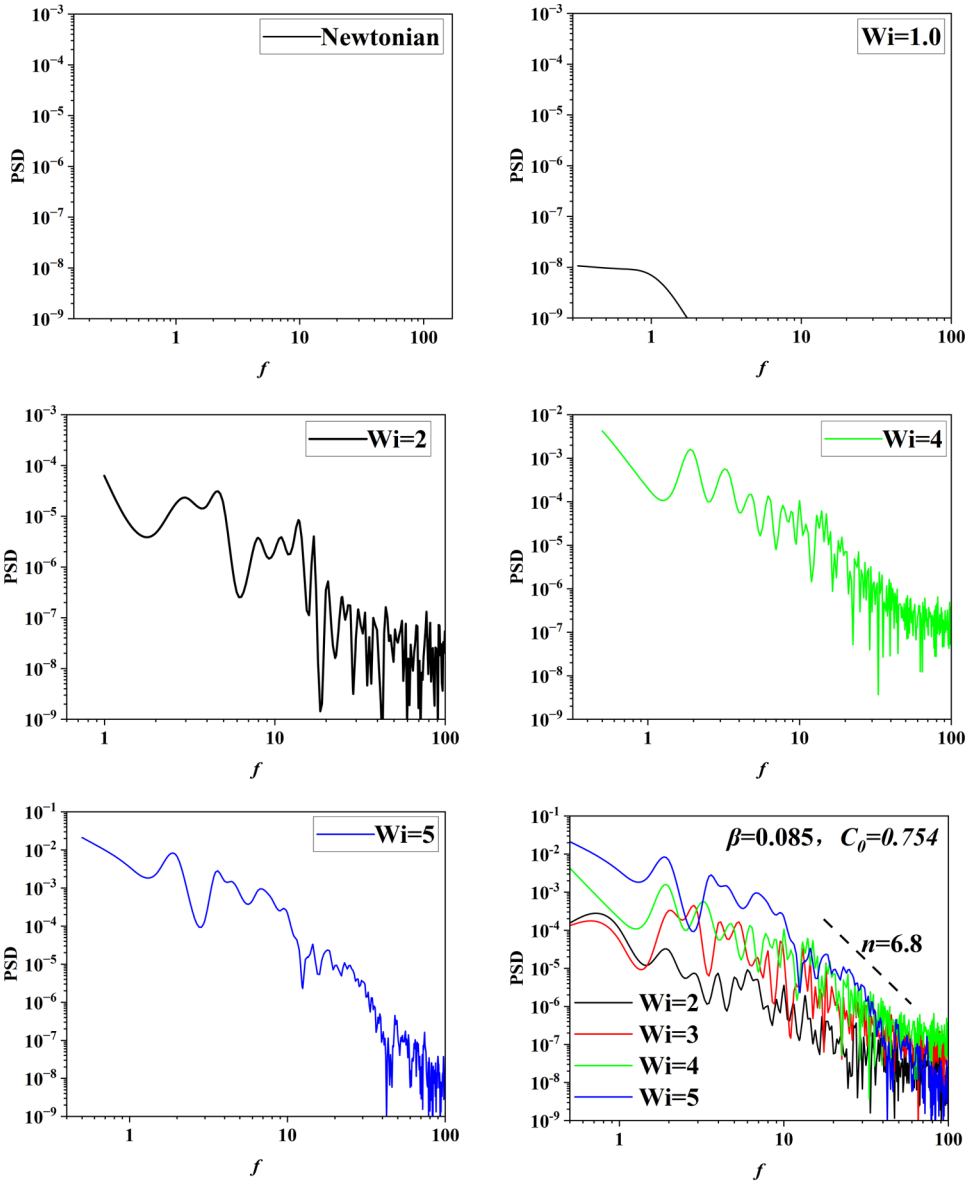

(a) β=0.085, C_0 = 0.754

FIG. 10. Power spectrum characteristics under a variety of operating regimes, with the electroelastic instability influenced by different polymer elasticities (*Wi* from 0 to 5).

with the exponent of EC instability reported in Refs. [43,60]. After exceeding the critical value $Wi = 3$, the exponent appears to be fixed at $n = 4.8$, which is slightly higher than the $n = 4$ reported by Pimenta and Alves [41]. In this section, the transition from a nearly flat PSD to a power-law PSD is accompanied by a decrease in the power-law exponents. That is, our results suggest a transition path from periodic oscillations, quasiperiodic oscillations, steady state, EHD chaos to elastic chaos in the ohmic regime $C_0 = 6.05$.

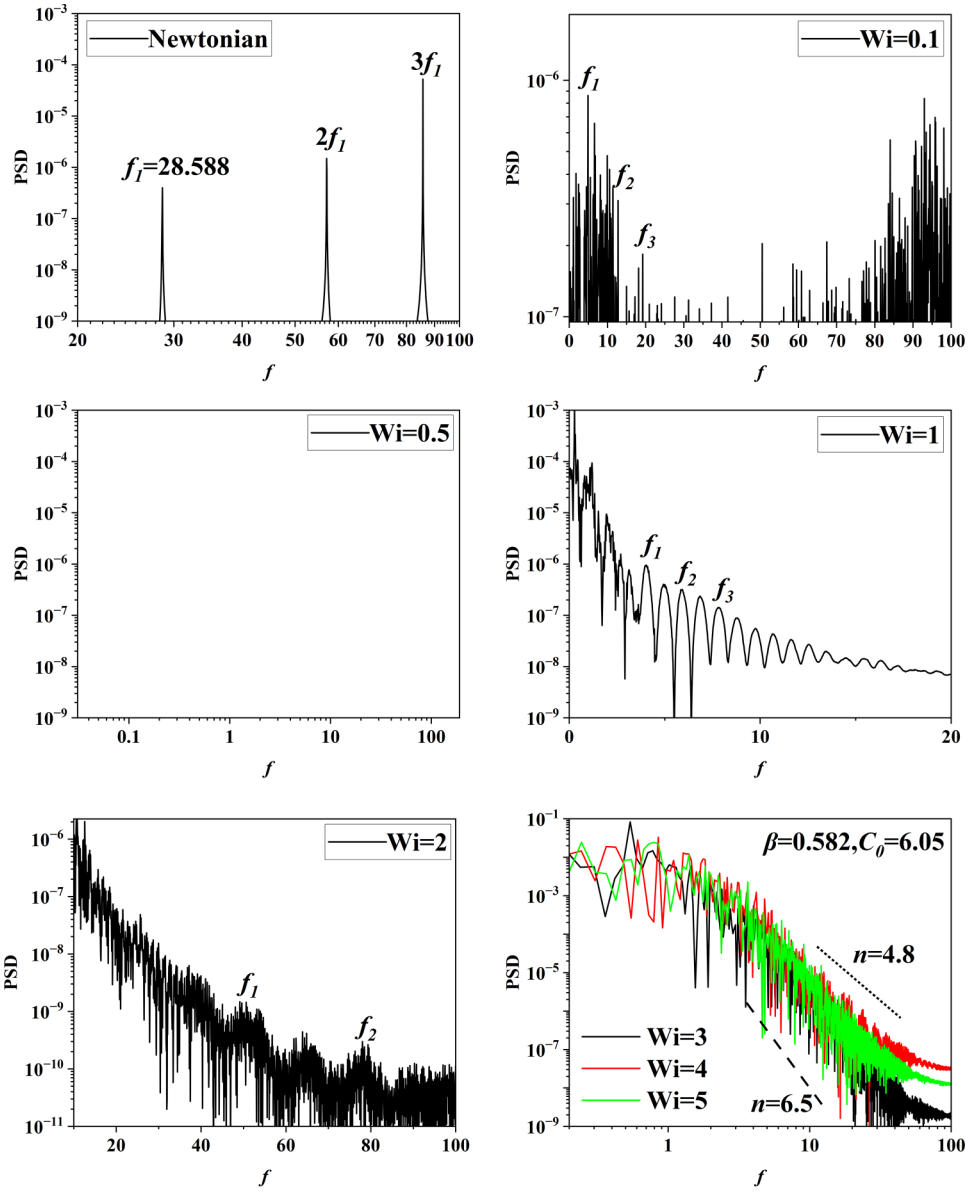

(b) β=0.582, C_0 = 6.05

FIG. 10. *(Continued.)*

In addition, the log-log plot of PSD at the monitoring point is presented to verify the flow behavior and instability for the remarkable ohmic regime ($C_0 = 12.07$). A broad continuous frequency range with power-law spectral scaling behavior can be seen in Fig. 10(c). The exponent $n = 4.1$ (at $Wi > 1$) is consistent with $n = 4.0$ or 3.7 reported in the literature [33]. It is also comparable with the power-law exponential decay of $n = 4$ for electroelastic instabilities in EOF cross-flow [41], demonstrating that it enters the flow behavior dominated by elastic instabilities. That is, the results show a direct transition path from quasiperiodic oscillations to elastic instability under the significant ohmic operating regime.

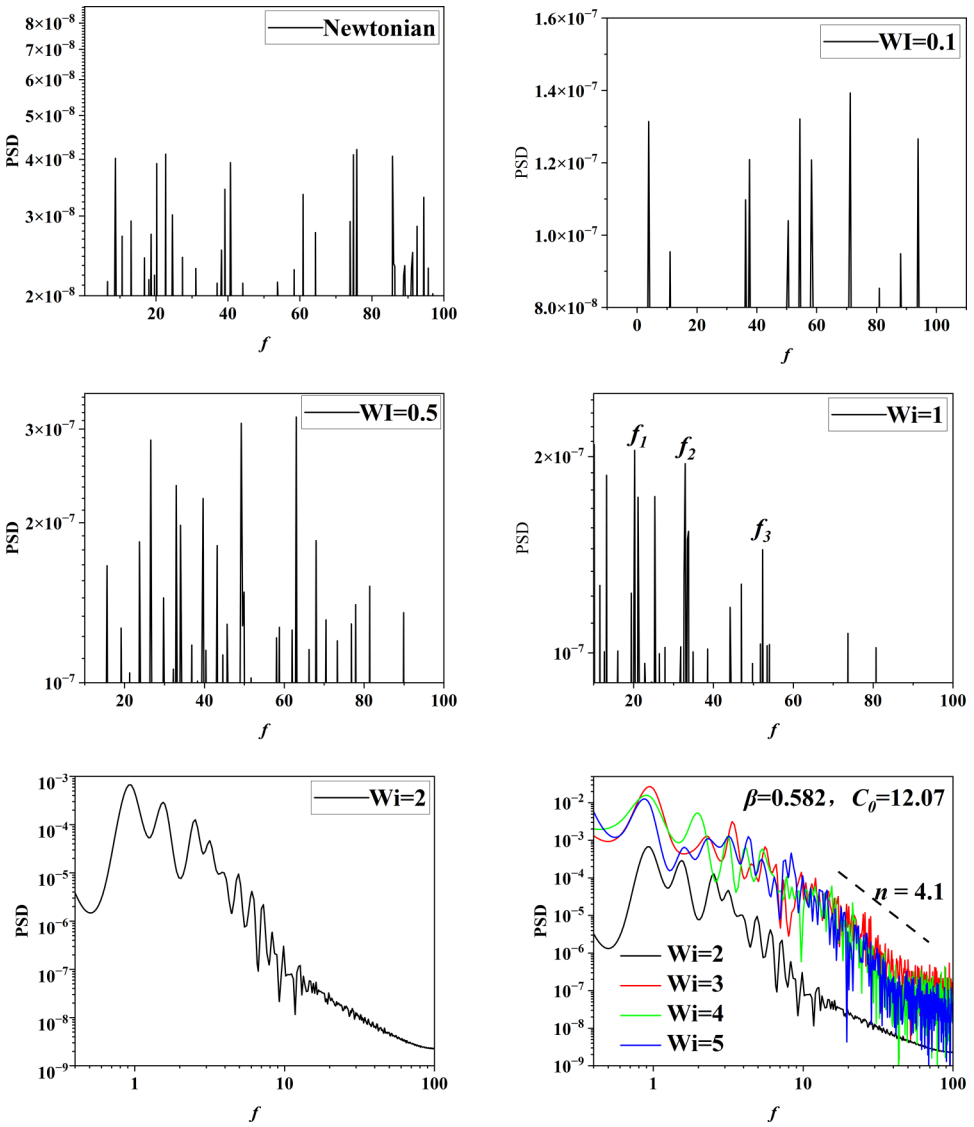

(c) β=0.582, C_0 = 12.07

FIG. 10. *(Continued.)*

C. Evaluation of elasticity effects on global characteristics

The field strength acts mainly on the ECF in the x direction due to the asymmetrical arrangement of the parallel electrodes in the vertical direction. To have an intuitive understanding of the instability mechanism underlying convection, elastic stress, and electric force, we use the momentum equation in the horizontal x direction:

$$\rho_m\left(\frac{\partial u_x}{\partial t}+u_x\frac{\partial u_x}{\partial x}+u_y\frac{\partial u_x}{\partial y}\right)=-\frac{\partial p}{\partial x}+\eta_s\left(\frac{\partial^2 u_x}{\partial x^2}+\frac{\partial^2 u_x}{\partial y^2}\right)+\left(\frac{\partial \tau_{xx}}{\partial x}+\frac{\partial \tau_{yx}}{\partial y}\right)+\rho_E E_x. \quad (30)$$

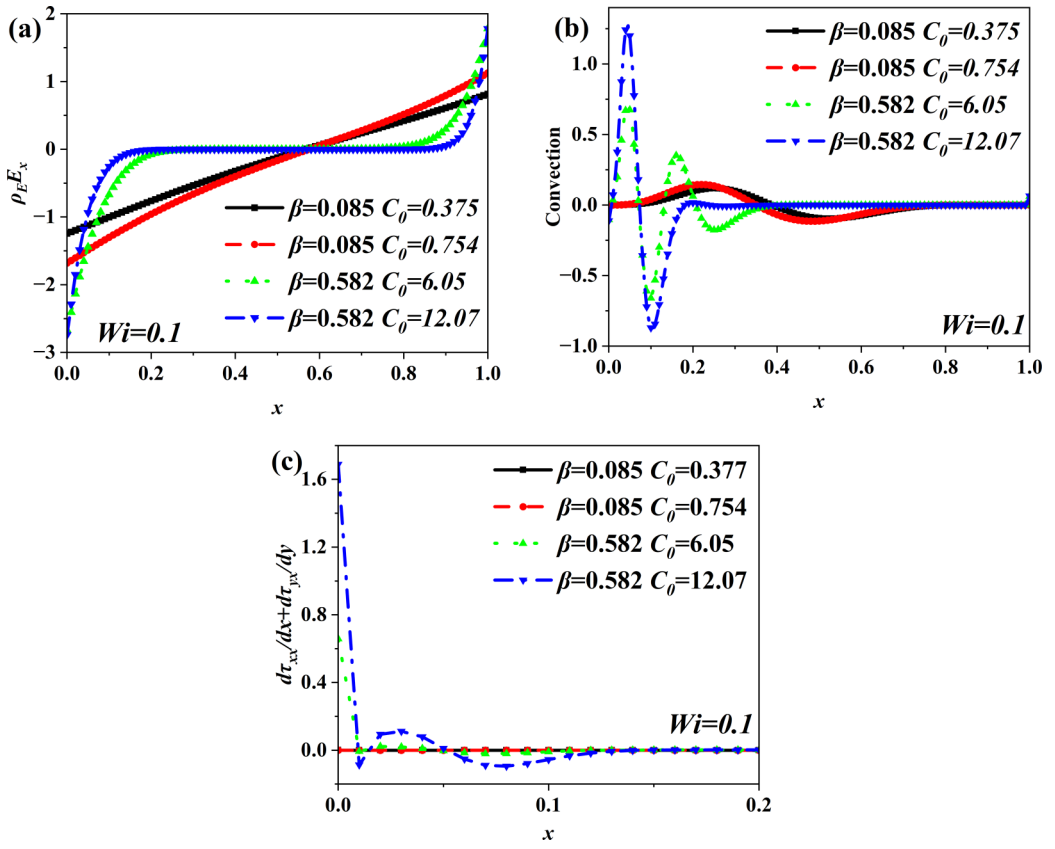

FIG. 11. The dynamic characteristics in the saturation and ohmic regimes. (a) The electrostatic force, (b) convection, and (c) elastic force, with a fixed polymer elasticity $Wi = 0.1$.

The left-hand side $\rho_m(\frac{\partial u_x}{\partial t} + u_x\frac{\partial u_x}{\partial x} + u_y\frac{\partial u_x}{\partial y})$ reflects the momentum increment per unit volume of fluid per unit time, where $\rho_m(u_x\frac{\partial u_x}{\partial x} + u_y\frac{\partial u_x}{\partial y})$ represents the acceleration caused by the inhomogeneity of the flow field, also known as the convective term; $-\frac{\partial p}{\partial x}$ represents the pressure acting on the volume element; $\eta_s(\frac{\partial^2 u_x}{\partial x^2} + \frac{\partial^2 u_x}{\partial y^2})$ represents the component of the viscous force; $\frac{\partial \tau_{xx}}{\partial x} + \frac{\partial \tau_{yx}}{\partial y}$ represents the component of the EF in the x direction; and $\rho_E E_x$ is the x component of the CF.

In the saturation regime $C_0 < 1$ [maintaining a constant polymer elasticity $Wi = 0.1$ in Fig. 11(a)], the net charge density is distributed throughout the bulk due to the overlapping DSLs, and the convective effect is significant in DSLs, which may be more inclined to develop inertia-leading EHD instability flow. Due to strong Coulomb driving forces, the elastic effect is suppressed and approaches a very small value throughout the bulks in Fig. 11(c). However, when the thickness of the DSLs (weak electric field, $C_0 = 12.07$) in the ohmic regime in Fig. 11(a) is smaller, the CFs are mainly concentrated inside the nonoverlapping DSLs in the ohmic regime, with a remarkable convective effect in the DSLs. Due to the small value of the CF competing with the high elastic stress, the bulk volume develops a high EF in the ohmic regime. Therefore, working in the ohmic regime is more likely to develop purely elastic instability flow [48], at least in the non-DSL region where very small CF effects are present. Under the same β parameter, the large C_0 corresponds to the amplitude of convective acceleration and elastic stress in DSLs/bulks. Therefore, the larger the C_0 value, the wider the electroneutral volume is to make viscoelastic molecules relax and release energy with an equal β number.

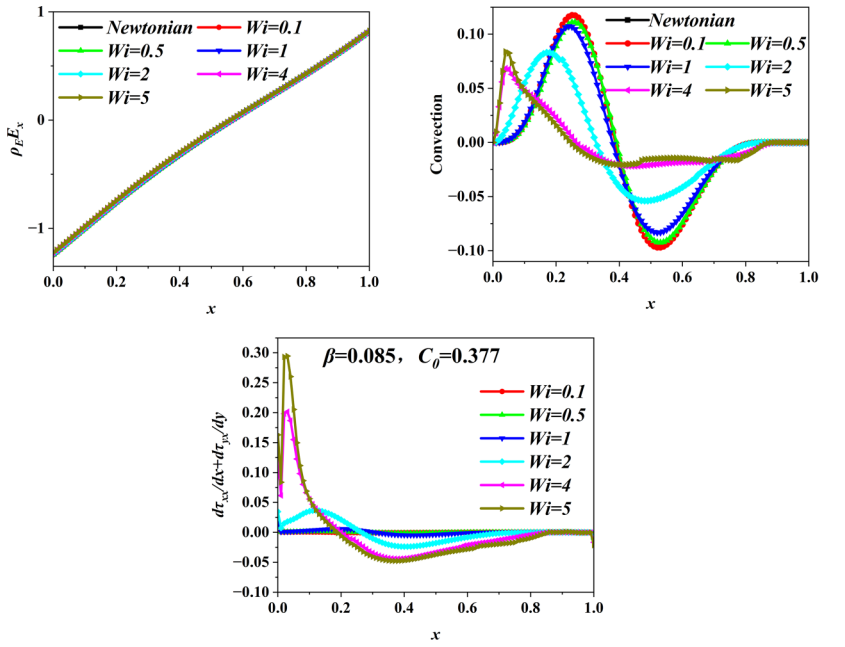

(a)

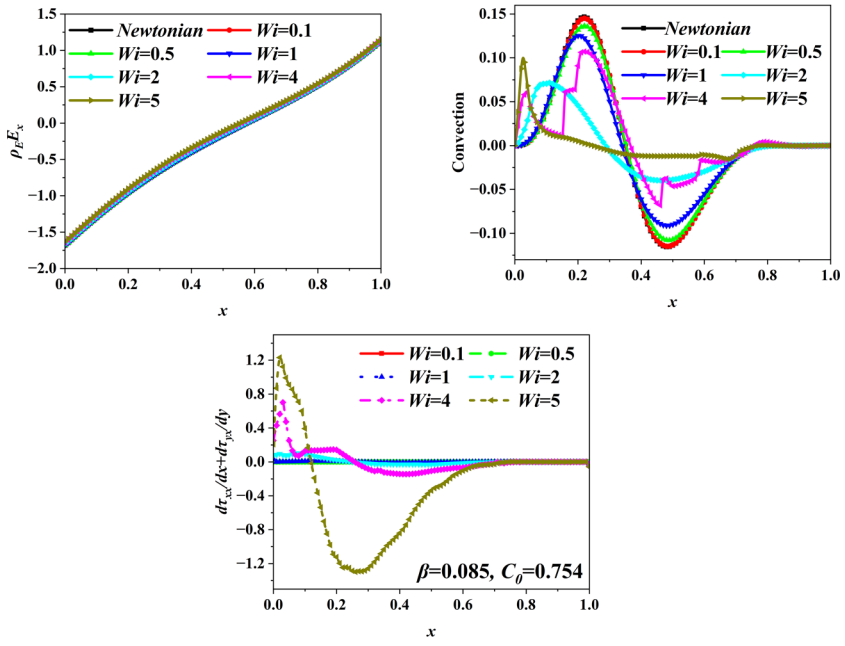

(b)

FIG. 12. Influence of polymer elasticity on the dynamic characteristics of the flow field. (a) Strong saturation regime, $\beta = 0.085$, $C_0 = 0.377$. (b) Weak saturation regime, $\beta = 0.085$, $C_0 = 0.754$.

Comparing the two saturation cases in Fig. 12, both have similar trends in the distribution of CFs, convection, and EF characteristics. Under strong saturation ($C_0 = 0.377$), the polymer has a negligible effect on the CF because the charge density formation mechanism is dominated by the

TABLE II. Variation in elastic stress and CF amplitude with polymer elasticity.

Fluid	$C_0 = 0.754$, CF	$C_0 = 0.754$, EF	$C_0 = 6.05$, CF	$C_0 = 6.05$, EF
Newtonian fluids	1.682	0	2.66848	0
$Wi = 0.1$	1.682	8.19×10^{-6}	2.66848	1.6335
$Wi = 0.5$	1.67982	7.10×10^{-4}	2.65226	2.315
$Wi = 1$	1.67982	0.07466	2.65014	3.050
$Wi = 2$	1.66173	0.20581	2.63489	4.045
$Wi = 4$	1.63974	1.4043	2.64059	8.363
$Wi = 5$	1.63132	2.46187	2.64153	22.18

ion transport term $z_{\pm}c_{\pm}K\mathbf{E}$. As shown in Fig. 12(a), the elastic stress is always lower than the value of the CF in the strong saturation regime ($C_0 = 0.377$); therefore, the ECF mode within the system is dominated by the CF. However, as the system shifts from the strong saturation regime ($C_0 = 0.377$) to the weak saturation regime ($C_0 = 0.754$), the magnitude of the elastic stress is progressively higher than the value of the CF as the polymer elasticity rises. Thus, the convective pattern in Fig. 12(b) is significantly altered. As the EF is not sufficient to fully suppress the effect of the CF under these conditions, an inertia-dominated EHD instability flow pattern is promoted.

Figure 13 illustrates the distribution of the flow dynamics in ohmic regimes. The comparison of Figs. 13(a) and 13(b) shows that the effect of polymer elasticity on the CF is more pronounced at high conduction number C_0 simply because the CF is weakened at the same time that the ion convective term in $\mathbf{u}c_{\pm}$ becomes more pronounced. In general, the convective acceleration has a similar sinusoidal character within the DSL at low polymer elasticity ($Wi < 0.5$), showing an irregular pulsation distribution as the Wi number increases beyond 2. We explain the above phenomenon in two ways. First, elastic stresses and CFs do not always act in the same direction, and the synergistic relationship between the two ultimately determines the dominance and pattern of convective acceleration. Second, when the value of the EF can reach or even exceed the CF by orders of magnitude, the ECF within the system may be transformed into a pattern dominated by the EF. Therefore, recalling the characteristics under the saturation regime, the CF is always higher than the elastic stress due to the highly overlapping DSLs; thus, the flow pattern formed is inertia-dominated EHD chaos. For a more visual comparison of the data in the graphs, we also present a comparison of the maximum values of the CFs and EFs in Table II under different operating regimes. The above results suggest that the relative magnitude of the elastic stress to the CF significantly affects the ECF instability within the system, depending on whether it is dominated by CFs or elasticity stress.

The relationship between control parameters and stability characteristics has not yet been systematically addressed. Therefore, it is necessary to quantify the kinetic and elastic energy of the associated driving parameters. Unlike Newtonian fluids, polymers can store energy during stretching by the main flow and providing energy to the flow during relaxation. In other words, the finite fluid element in a viscoelastic fluid flow contains both kinetic and elastic energy. In addition, alternately stretching and relaxing the polymer (implying a change in the action of the polymer during flow) can act as a trigger for elastic instability [51,56]. Correspondingly, we plot the L^2-norm of the velocity field evolving–the kinetic energy for different Wi in Fig. 14, defined as

$$E_k = \frac{1}{2V_t}\int |\mathbf{u}|^2 dV = \frac{1}{2V_t}\sum_{k=1}^{N} |\mathbf{u}_k|^2 V_k = \frac{1}{2N}\sum_{k=1}^{N} |\mathbf{u}_k|^2, \tag{31}$$

where N is the number of cells of the mesh, and $V_t = NV_k$ for a uniform mesh. As follows, E_{k0} represents the time-averaged kinetic energy of the system for the Newtonian fluid. Correspondingly,

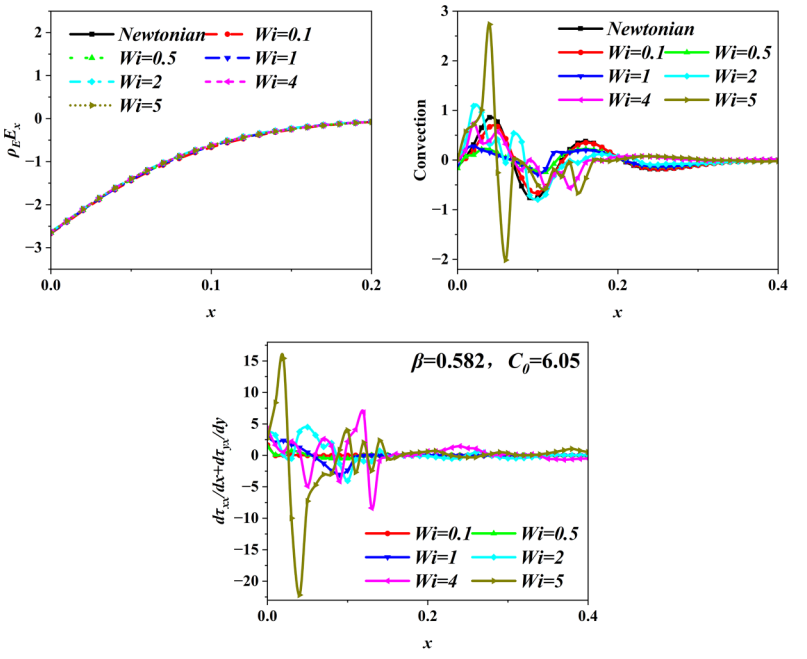

(a)

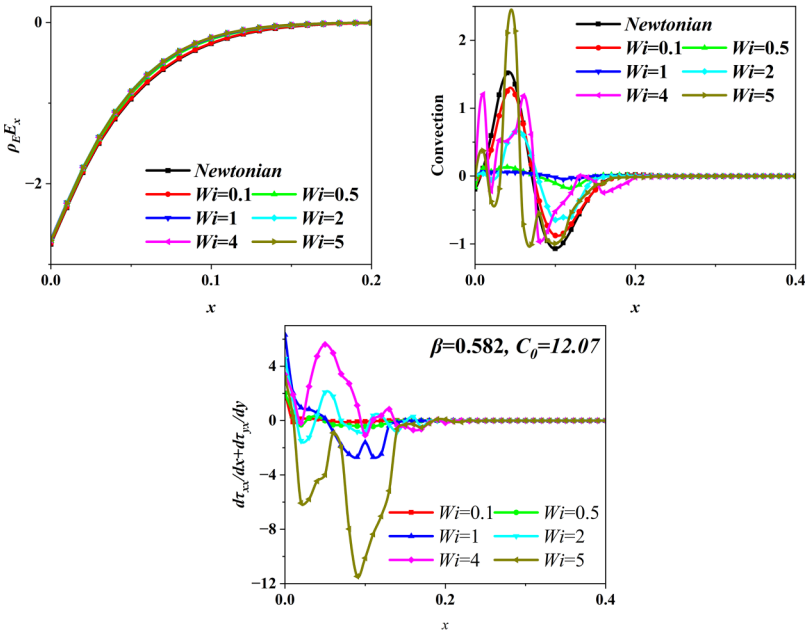

(b)

FIG. 13. Effect of polymer elasticity on the dynamic characteristics of the flow field. (a) Ohmic regime, $\beta = 0.582$, $C_0 = 6.05$. (b) Ohmic regime, $\beta = 0.582$, $C_0 = 12.07$.

the elastic energy can be written as

$$E_p = \frac{1}{2V_t}\int \frac{\lambda}{\eta_p} tr(\boldsymbol{\tau}) dV = \frac{1}{2V_t}\sum_{k=1}^{N} \frac{\lambda}{\eta_p} tr(\boldsymbol{\tau}_{\mathbf{k}}) V_k = \frac{1}{2N}\frac{\lambda}{\eta_p}\sum_{k=1}^{N} tr(\boldsymbol{\tau}_{\mathbf{k}}). \tag{32}$$

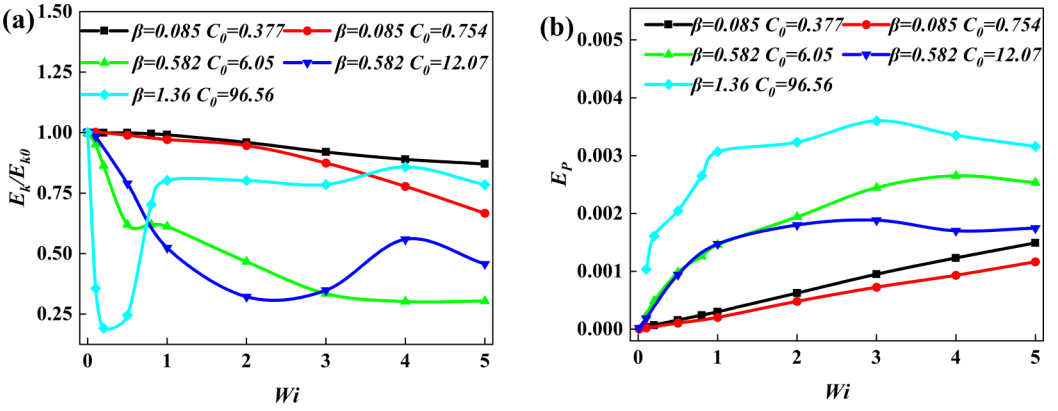

FIG. 14. The effect of the Weissenberg numbers on global quantities of the system, (a) time-averaged kinetic energy, and (b) time-averaged elastic energy of the system.

At $\beta = 0.085$, the kinetic energy in Fig. 14(a) decreases approximately linearly, and most of the molecules are stretched, accompanied by the conversion of kinetic energy into elastic energy to be stored. As the elastic energy rises nonlinearly, there are two cases (e.g., $\beta = 1.360$, $C_0 = 96.56$, and $\beta = 0.582$, $C_0 = 12.07$) where the average kinetic energy is partially recovered at $Wi = 1$ and 3, respectively, probably due to partial relaxation of polymer molecules. The decay of the kinetic energy, accompanied by a rise in the elastic energy in the saturation regime, also shows increased RMS fluctuations in Figs. 7(a) and 7(b) for the elastic instability condition. This is because the rise in elastic energy within the system (at high Wi numbers) leads to an increase in the chaotic elements within the system, which exacerbates the velocity RMS fluctuations. The RMS fluctuations of inertia-dominated EHD instability in the ohmic regime are shown to be partially suppressed due to the competing CFs and elastic stresses at lower Wi numbers, as shown in Figs. 7(c) and 7(d).

Correspondingly, the elastic energy shows a linear trend at β=0.085 in Fig. 14(b), satisfying the relationship $Ep = tr(Wi \cdot \frac{1}{1-\chi})$. In contrast, a transition from the CF to an elastic inertia-dominated state can be observed at $\beta = 0.582$ in Fig. 10(b), with the elastic energy showing a nonlinear increase in Fig. 14(b). This is mainly due to several factors: relatively weak driving forces, sufficient relaxation of polymer molecules (at intermediate sizes), comparable stabilizing and destabilizing forces, elastic bursts, etc. It is worth mentioning that the E_p curves are approximately linear in the ohmic regime at low Wi numbers. However, as the Wi number increases, the elastic energy is partially converted into kinetic energy, and E_p flattens out. With $\beta = 1.360$ and $C_0 = 96.56$, the kinetic energy decreases sharply with rapid E_p accumulation even for weak elasticity $Wi < 1$. This means that a suitable polymer stress relaxation distance (in medium dimensionless sizes) and C_0 value (operating in the ohmic regime) can significantly change the energy gain and loss effect in the EHD system. In summary, the increase in size leaves sufficient relaxation time and distance for molecular recovery, bringing forward the equilibrium state of elastic energy and kinetic energy in the system.

D. Transition to chaotic flow

To fully elucidate the relationship between the different flow patterns and control parameters, many numerical simulations have been carried out over a wide range of parameters ($0.377 \leqslant C_0 \leqslant 193$, $0 \leqslant Wi \leqslant 5$, and $0.085 \leqslant \beta \leqslant 1.36$). The β parameter quantifies the effects of size limitation and field-enhanced dissociation. Here, C_0 is inversely proportional to the field strength E, reflecting

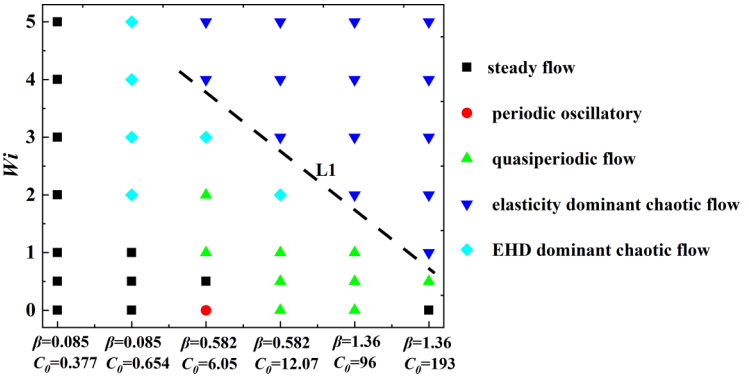

FIG. 15. Flow pattern diagrams of the conduction electroconvective flow (ECF) of a viscoelastic dielectric liquid, in which the black square represents steady flow, the red circle represents periodic flow, the upper triangle represents quasiperiodic flow, the lower triangle represents elasticity-dominant chaotic flow, and the diamond represents electrohydrodynamic (EHD)-dominant chaotic flow. Parameter range: $0.377 \leqslant C_0 \leqslant 193$, $0 \leqslant Wi \leqslant 5$, $0.085 \leqslant \beta \leqslant 1.36$.

the influence of Coulomb driving forces. The flow pattern of the conduction ECF of a viscoelastic dielectric liquid can be divided into five subregions in Fig. 15. The steady flow is widespread for small β, spanning the entire range of polymer elasticity researched. As β (or C_0) increases, the flow distribution deviates significantly further from the steady state. Periodic oscillatory flow only occurs at a moderate size ($\beta = 0.582$) in our results due to the insufficient number of selected cases. With increasing β (or C_0), quasiperiodic and intermittent oscillatory flows can develop at low Wi numbers with multiple incommensurable frequencies. Due to the sufficient size relaxation distance for large β (1.36) with weak electric field contribution C_0, chaotic flow patterns appear at a lower $Wi = 1$, which is dominated by elastic nonlinearity. At small β (0.085), the transition from steady state to EHD-dominated chaotic flow (in the inertially dominated regime) occurs with increased polymer elasticity. The dashed line L1 divides the EHD-dominated flow pattern from the elastic-dominated instability flow. As shown in Fig. 14, under the same β parameters (by adjusting d), the time-averaged kinetic energy and elastic energy are different with different C_0 (adjusting electric field intensity). In Fig. 15, with a continuous sequence of C_0 and different β parameters, the transition sequence has different paths. This is because the β parameter changes the molecular relaxation distance in the bulk of the system, while C_0 changes the CF in the system and the thickness of the DSLs. The above results once again emphasize the competition and promotion mechanism of elasticity, inertia nonlinearity, and CF in the development of flow instability. Obviously, the flow pattern transitions around $C_0 = 1$ may be more important [48]. However, the extracted cases in our results from saturation to the ohmic regime are not sufficient, and more detailed settings are left for future research.

V. CONCLUSIONS

Based on our previous study [48], we investigate the mechanism of EHD conduction driving for non-Newtonian dielectric fluids described by the Oldroyd-B model in this paper. The effects of different operating regimes and polymer elasticity are discussed. Viscoelasticity leads to new instability patterns and richer dynamic behaviors in conduction ECF systems. However, these phenomena are absent for Newtonian fluids. The remaining conclusions are as follows:

For a small value of β ($=0.085$), the system operates under the saturation regime, regardless of the high or low magnitude of the voltage. As β increases (at $\beta = 0.582$), the system may shift from the ohmic to the saturation regime with the change in field strength. Moreover, for $\beta > 1$, the system operates in the ohmic regime even at very high voltages ($\Delta\phi = 10.0$ kV), where electric-

field-enhanced dissociation occurs more strongly. The Onsager-Wien effect acts weakly at low β values and can be significant at high β values, maintaining a significant electroneutral bulk.

We also analyze the rich structural changes in the flow field and the complex nonlinear dynamics during the transition from steady state to periodic oscillations and finally to chaotic states. The time evolution of $U_{\max}$ shows that the polymer elasticity significantly influences the flow stability in the ohmic regime, assessed by the RMS amplitude of oscillation. The vortexes still show clear symmetry with weak elasticity. However, when the *Wi* number reaches a critical value, symmetry is completely lost due to the occasional burst element of elasticity [51], and the flow field enters the elastic instability domain. The transition sequences are discussed in the saturation and ohmic regimes. The system is ultimately steady state for several *Wi* conditions in the strong saturation regime $C_0 = 0.377$. The path from steady-state transition to inertia-dominated EHD chaos is observed for the system in a weak saturation regime $C_0 = 0.754$. The transition path is from periodic oscillations, quasiperiodic oscillations, steady state, EHD chaos to elastic chaos in the ohmic regime $C_0 = 6.05$. In the remarkable ohmic operating regime ($C_0 = 12.07$), the exponent $n = 4.1$ (at $Wi > 1$) is consistent with $n = 4.0$ or 3.7 reported in the literature [33]. It is also comparable with the power-law exponential decay of $n = 4$ for electroelastic instabilities in electroosmotic cross-flow [41], demonstrating that it enters the flow behavior dominated by elastic instabilities.

The CFs are mainly concentrated inside the nonoverlapping DSLs in the ohmic regime, with a remarkable convective effect in DSLs. Due to the small value of the CF competing with the high elastic stress, the bulk volume shows a high EF in the ohmic regime. Therefore, working in the ohmic regime is more likely to develop purely elastic instability flow. The elastic stresses and CFs do not always act in the same direction, and the synergistic relationship between the two ultimately determines the convective pattern. When the value of the EF can reach or even exceed the CF by orders of magnitude, the ECF within the system may be transformed into elastic chaos flow. The CF is always higher than the elastic stress due to the highly overlapping DSLs under the saturation regime; thus, the flow pattern formed is inertia-dominated EHD chaos. We also quantify the kinetic and elastic energy of the associated driving parameters, and the flow patterns are mainly divided into five subregions.

In summary, this paper is the foundation for applying EHD conduction to complex fluid systems, such as crude oil pumping and cooling in-pipe flow. Additionally, the research reported here can provide a reference for applications of ECF, such as enhancement of mixing and heat transfer.

ACKNOWLEDGMENTS

This paper is supported by the National Natural Science Foundation of China (Grant No. 52076055) and the Fundamental Research Funds for the Central Universities (Grant No. FRFCU5710094020).

APPENDIX: IONIC AND NET CHARGE DENSITY DISTRIBUTION

Before discussing the different size effects of the EHD conduction phenomenon, it is necessary to analyze two operating regimes in depth. Figure 16 shows the net charge density distribution and the concentration (positive and negative ions) distribution at different reference lengths. The conduction number C_0 characterizes a ratio of two typical times, the ion transport time $t_K = d/KE_0$ and the ohmic time $t_\sigma^0 = \varepsilon/\sigma_0$. The former refers to the time for an ion to drift from one electrode to the counterelectrode, while the latter refers to the time for an ion to recombine without electric field reinforcement:

$$C_0 = \frac{e_0 c_0 d^2}{\varepsilon \Delta\phi} = \frac{\sigma_0 d^2}{2\varepsilon K \Delta\phi} = \frac{d^2/(K\Delta\phi)}{\varepsilon/\sigma_0} = \frac{\tau_K}{2\tau_\sigma^0}. \tag{A1}$$

Consider the Onsager-Wien effect [21,27] with a variation ohmic time of the form $\tau_\sigma = \varepsilon/\sigma = \tau_\sigma^0\sqrt{F(b)}$, where $\sigma = \sigma_0\sqrt{F(b)}$ and $F(b) = 1 + 2\beta^2 E^*/C_0$. Here, σ_0 represents the conductivity

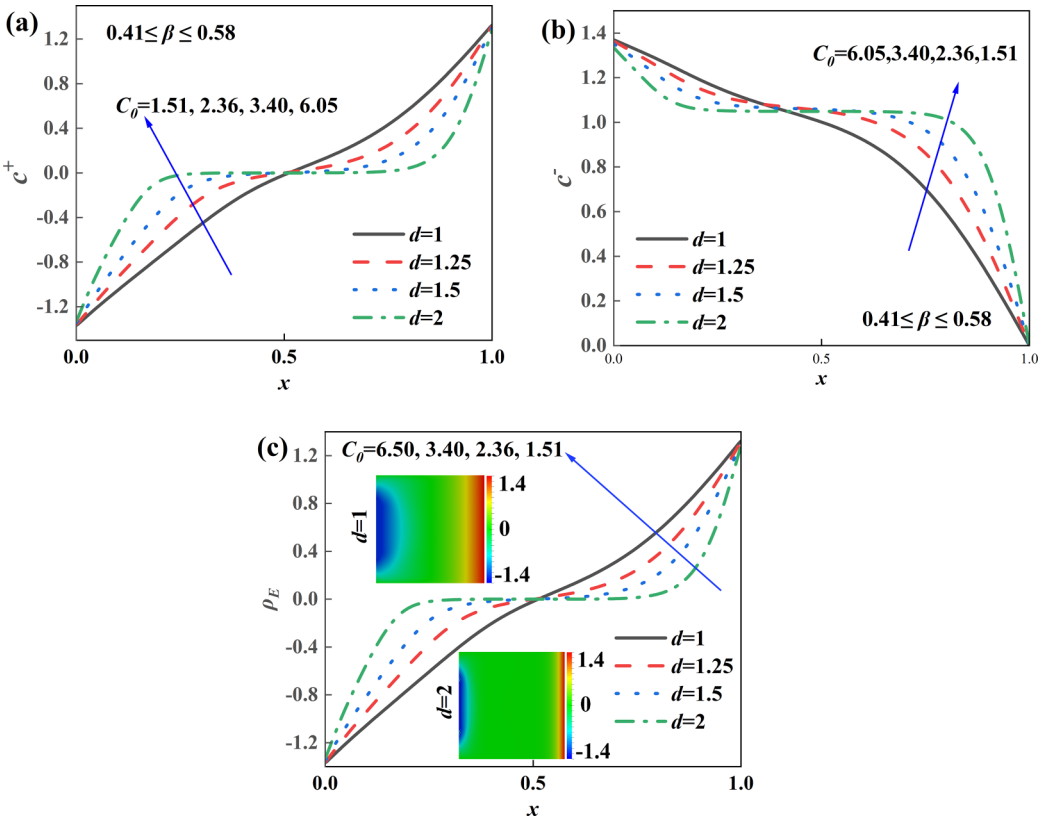

FIG. 16. Ionic distribution and net charge density distribution, (a) cation concentration, (b) anion concentration, and (c) net charge density, maintaining $Wi = 0$ and $\Delta\phi = 1$ kV.

without electric-field-enhanced dissociation. In general, the conductivity of dielectric liquids ranges from 10^{-11} to 10^{-7} S/m, and it is widely used in numerical and experimental studies. We can then obtain the distance of movement required for the ion to undergo recombination near the electrode:

$$\lambda_H \simeq KE_0\tau_\sigma^0 = \frac{d}{2C_0\sqrt{F(b)}} = \frac{d}{2C_0^E}, \tag{A2}$$

where $F(b) = \sum_{n=0}^{\infty} \frac{b^{2n}}{n!(n+1)!} = \sum_{n=0}^{\infty} \frac{(4OE)^n}{n!(n+1)!}$ is generally >1 under the Onsager-Wien effect. The parameter $O = e_0^3/(16\pi\varepsilon_0\varepsilon_r k_B^2 T^2)$ denotes the Onsager constant, and $b = 2\sqrt{OE}$ functions the field intensity $E = |\mathbf{E}|$. When $C_0 \ll 1$, it is $\tau_0^\sigma \gg \tau_k$ and $\lambda_H \gg d$, and no electroneutral bulk indicates DSL overlap. The formation of the saturation regime occurs because the free charge has left the liquid before recombination occurs, so there are few net charge densities $[\rho_E = e(c_+ - c_-)]$ in the bulk. When $C_0 \gg 1$, we have to know $\tau_0^\sigma \ll \tau_k$ and $\lambda_H \ll d$, operating in the ohmic regime, which indicates that ions have time to recombine inside the volume. Figure 16 illustrates the ion concentration and net charge density showing multiple conduction numbers C_0 and different ranges of β values. Different values of d determine the parameter β, ranging from <1 on the microscale to tens of orders of magnitude on the centimeter scale. The dividing line is well represented in Fig. 16 between the DSLs and the electroneutral bulk, and the relative thickness of the DSL (λ_H/d) tends to decrease as C_0 increases, as seen from Eq. (A2), where $C_0^E = C_0\sqrt{F(b)}$ is inversely proportional to C_0. It is also worth noting that $C_0^E = C_0\sqrt{F(b)}$ depends heavily on C_0; as d increases or C_0 increases, C_0^E can also be expected to have a significant upward trend with increasing d and decreasing

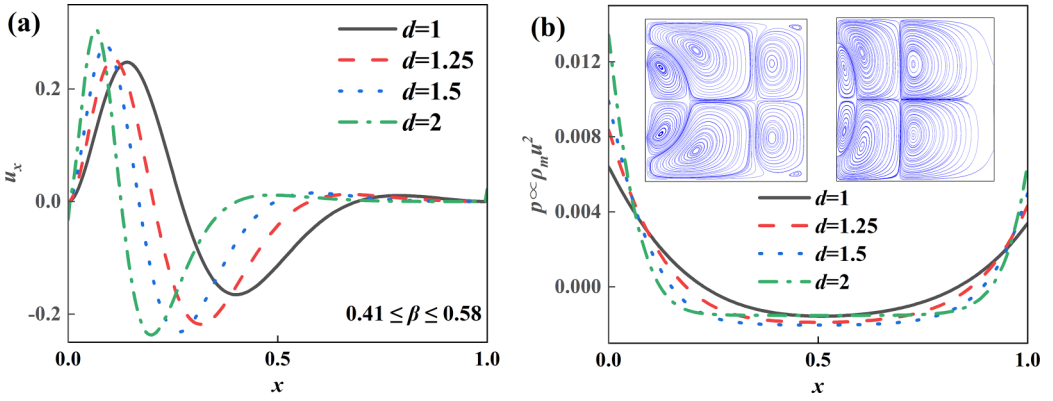

FIG. 17. Velocity trend and the pressure difference between positive and negative electrodes, maintaining $Wi = 0$ and $\Delta\phi = 1$ kV.

DSL thickness. Furthermore, the same potentials are shown in Fig. 16, and β ($0.41 \leqslant \beta \leqslant 0.58$) at different reference scales d are comparable and will not be analyzed in too much detail here.

The above analysis shows two DSLs close to the electrodes and an electroneutral region within the ohmic regime for $C_0^E > 1$. The net charge density and field gradient within the DSLs lead to a limiting value of the CF ($\rho_E E$). Due to the interaction of the fluid viscous forces with the CF, the driving effect is expected to occur near the electrodes, acting further on the fluid and generating flow. Figure 17 illustrates the velocity profile and pressure distribution along the centerline between the positive and negative electrodes in the square cavity. In the insets of Fig. 17(b), the flow diagrams are shown for $d = 1$ and 2. At $d = 1$ mm, two vortices can be seen to form symmetrically near the positive and negative electrodes. Due to the asymmetry of the electrodes in this paper, there is a significant difference in the size of the vortices formed near the electrodes. Furthermore, the symmetrical interlayer vortices shown in the streamlines are formed due to the migration of positive and negative ions to different electrodes in the electroneutral bulk. With $d = 1$ changing to $d = 2$, the area of action of the vortex pair near the negative electrode increases, and the vortex pair near the positive electrode decreases because of the net charge density gradient (negative side) increasing with d. Furthermore, Fig. 17(a) shows that the relative positions of the velocity maxima and minima on the anode side appear to be closer to the pole plate as d increases, which is consistent with the trend of decreasing vortex pair size near the positive pole plate shown in Fig. 17(b), insets. The pressure characteristics shown in Fig. 17(b), with a balance of viscous and electric forces, have limiting values for the net charge density accumulated inside the DSL, resulting in a large pressure gradient described as $\Delta p \sim \rho_E \cdot E \cdot \Delta x$.

[1] V. K. Patel and J. Seyed-Yagoobi, Long-term performance evaluation of microscale two-phase heat transport device driven by EHD conduction, IEEE Trans. Ind. Appl. **50**, 3011 (2014).

[2] M. Talmor and J. Seyed-Yagoobi, Numerical study of micro-scale EHD conduction pumping: The effect of pump orientation and flow inertia on heterocharge layer morphology and flow distribution control, J. Electrost. **111**, 103548 (2021).

[3] N. Nourdanesh and E. Esmaeilzadeh, Experimental study of heat transfer enhancement in electrohydrodynamic conduction pumping of liquid film using flush electrodes, Appl. Therm. Eng. **50**, 327 (2013).

[4] J. S. Yagoobi, Transport of heat and mass with electrical field—From Earth to space, *2019 IEEE 20th International Conference on Dielectric Liquids (ICDL)* (IEEE, Rome, 2019), pp. 1–5.

[5] D. Fernandes and Y. Suh, Numerical simulation and design optimization of an electrohydrodynamic pump for dielectric liquids, Int. J. Heat Fluid Flow **57**, 1 (2016).
[6] V. Cacucciolo, H. Shigemune, M. Cianchetti, C. Laschi, and S. Maeda, Conduction electrohydrodynamics with mobile electrodes: A novel actuation system for untethered robots, Adv. Sci. **4**, 1600495 (2017).
[7] Y. Guan and I. Novosselov, Numerical analysis of electroconvection in cross-flow with unipolar charge injection, Phys. Rev. Fluids **4**, 103701 (2019).
[8] A. Castellanos, *Electrohydrodynamics* (Springer Science & Business Media, Wien, 1998).
[9] V. Cacucciolo, J. Shintake, Y. Kuwajima, S. Maeda, D. Floreano, and H. Shea, Stretchable pumps for soft machines, Nature (London) **572**, 516 (2019).
[10] V. K. Patel, F. Robinson, J. Seyed-Yagoobi, and J. Didion, Terrestrial and microgravity experimental study of microscale heat-transport device driven by electrohydrodynamic conduction pumping, IEEE Trans. Ind. Appl. **49**, 2397 (2013).
[11] M. Daaboul, P. Traoré, P Vázquez, and C. Louste, Study of the transition from conduction to injection in an electrohydrodynamic flow in blade-plane geometry, J Electrostat. **88**, 71 (2017).
[12] Y. Feng and J. Seyed-Yagoobi, Electrical charge transport and energy conversion with fluid flow during electrohydrodynamic conduction pumping, Phys. Fluids **19**, 057102 (2007).
[13] S. I. Jeong, J. Seyed-Yagoobi, and P. Atten, Theoretical/numerical study of electrohydrodynamic pumping through conduction phenomenon, IEEE Trans. Ind. Appl. **39**, 355 (2003).
[14] P. Atten and J. Seyed-Yagoobi, Electrohydrodynamically induced dielectric liquid flow through pure conduction in point/plane geometry, IEEE Trans. Dielectr. Electr. Insul. **10**, 27 (2003).
[15] Y. I. Kharkats, The mechanism of "supralimiting" currents at ion-exchange membrane/electrolyte interfaces, Sov. Electrochem. **21**, 7 (1986).
[16] I. Rubinstein and B. Zaltzman, Electro-osmotically induced convection at a permselective membrane, Phys. Rev. E **62**, 2238 (2000).
[17] M. B. Andersen, M. Van Soestbergen, A. Mani, H. Bruus, P. M. Biesheuvel, and M. Z. Bazant, Current-Induced Membrane Discharge, Phys. Rev. Lett. **109**, 108301 (2012).
[18] V. V. Nikonenko, A. V. Kovalenko, M. K. Urtenov, N. D. Pismenskaya, J. Han, P. Sistat, and G. Pourcelly, Desalination at overlimiting currents: State-of-the-art and perspectives, Desalination **342**, 85 (2014).
[19] C. Druzgalski and A. Mani, Statistical analysis of electroconvection near an ion-selective membrane in the highly chaotic regime, Phys. Rev. Fluids **1**, 073601 (2016).
[20] J. C. Ryu, H. J. Park, J. K. Park, and K. H. Kang, New Electrohydrodynamic Flow Caused by the Onsager Effect, Phys. Rev. Lett. **104**, 104502 (2010).
[21] D. Fernandes, D. Cho, and Y. Suh, Electrohydrodynamic flow of dielectric liquid around a wire electrode-effect of truncation of Onsager function, IEEE Trans. Dielectr. Electr. Insul. **21**, 194 (2014).
[22] Y. Suh and K. Baek, Competition between the bulk and the dissociation layer in electrohydrodynamic flow of dielectric liquid around coplanar electrodes, Phys. Rev. E **87**, 023009 (2013).
[23] W. Kim, J. C. Ryu, Y. K. Sun, and K. H. Kang, Pumping of dielectric liquids using non-uniform-field induced electrohydrodynamic flow, Appl. Phys. Lett. **99**, 224102 (2011).
[24] L. Wang, Z. Wei, T. Li, Z. Chai, and B. Shi, A lattice Boltzmann modelling of electrohydrodynamic conduction phenomenon in dielectric liquids, Appl. Math. Modell. **95**, 361 (2021).
[25] Y. Feng and J. Seyed-Yagoobi, Understanding of electrohydrodynamic conduction pumping phenomenon, Phys. Fluids **16**, 2432 (2004).
[26] Y. Suh, K. Baek, and D. Cho, Asymptotic and numerical analysis of electrohydrodynamic flows of dielectric liquid, Phys. Rev. E **88**, 023003 (2013).
[27] P. A. Vázquez, M. Talmor, J. Seyed-Yagoobi, P. Traoré, and M. Yazdani, In-depth description of electrohydrodynamic conduction pumping of dielectric liquids: Physical model and regime analysis, Phys. Fluids **31**, 113601 (2019).
[28] Y. Y. Bao, J. H. Huang, Y. J. Chen, and Z. H. Liu, Natural convection heat transfer of nanofluid in a cavity under an inhomogeneous electric field, Int. J. Heat Mass Transfer **131**, 341 (2019).
[29] N. Nourdanesh, S. Hossainpour, and K. Adamiak, Numerical simulation and optimization of natural convection heat transfer enhancement in solar collectors using electrohydrodynamic conduction pump, Appl. Therm. Eng. **180**, 115825 (2020).

[30] H. Asadi Dereshgi, H. Dal, and M. Z. Yildiz, Piezoelectric micropumps: State of the art review, Microsyst. Technol. **27**, 4127 (2021).
[31] S. Sinnamon, Coolant distribution control in satellite structural panels using electrohydrodynamic conduction pumping, Master's Thesis, The University of New Mexico, 2012.
[32] P. A. Vazquez, J. Seyed-Yagoobi, P. Traore, and C. Louste, EHD Pumping in Flexible Conic Nozzle, *2019 IEEE 20th International Conference on Dielectric Liquids (ICDL)* (IEEE, Rome, 2019), pp. 1–4.
[33] P. Ballesta and M. Alves, Purely elastic instabilities in a microfluidic flow focusing device, Phys. Rev. Fluids **2**, 053301 (2017).
[34] G. Li, L. A. Archer, and D. L. Koch, Electroconvection in a Viscoelastic Electrolyte, Phys. Rev. Lett. **122**, 124501 (2019).
[35] B. Xu, Z. Gu, W. Liu, P. Huo, Y. Zhou, S. Rubinstein, M. Bazant, B. Zaltzman, I. Rubinstein, and D. Deng, Electro-osmotic instability of concentration enrichment in curved geometries for an aqueous electrolyte, Phys. Rev. Fluids **5**, 091701 (2020).
[36] L. Song, P. Jagdale, L. Yu, Z. Liu, D. Li, C. Zhang, and X. Xuan, Electrokinetic instability in microchannel viscoelastic fluid flows with conductivity gradients, Phys. Fluids **31**, 082001 (2019).
[37] F.-C. Li, Y. Dong, Y. Kawaguchi, and M. Oshima, Experimental study on swirling flow of dilute surfactant solution with deformed free-surface, Exp. Therm. Fluid Sci. **33**, 161 (2008).
[38] T. Hayat, S. Hina, and A. A. Hendi, Heat and mass transfer effects on peristaltic flow of an Oldroyd-B fluid in a channel with compliant walls, Heat Trans. Asian Res. **41**, 63 (2012).
[39] A. Taleb, H. BenHamed, M. Ouarzazi, and H. Beji, Analytical and numerical analysis of bifurcations in thermal convection of viscoelastic fluids saturating a porous square box, Phys. Fluids **28**, 053106 (2016).
[40] M. Yu, K. H. Ahn, and S. J. Lee, Design optimization of ink in electrohydrodynamic jet printing: Effect of viscoelasticity on the formation of Taylor cone jet, Mater. Des. **89**, 109 (2016).
[41] F. Pimenta and M. Alves, Electro-elastic instabilities in cross-shaped microchannels, J. Non-Newtonian Fluid Mech. **259**, 61 (2018).
[42] F. Li, S.-Y. Ke, X.-Y. Yin, and X.-Z. Yin, Effect of finite conductivity on the nonlinear behaviour of an electrically charged viscoelastic liquid jet, J. Fluid Mech. **874**, 5 (2019).
[43] Z.-G. Su, Y.-M. Zhang, K. Luo, and H.-L. Yi, Instability of electroconvection in viscoelastic fluids subjected to unipolar injection, Phys. Fluids **32**, 104102 (2020).
[44] Z.-G. Su, T.-F. Li, K. Luo, and H.-L. Yi, Nonlinear behavior of electrohydrodynamic flow in viscoelastic fluids, Phys. Rev. Fluids **6**, 093701 (2021).
[45] J. M. Crowley, G. S. Wright, and J. C. Chato, Selecting a working fluid to increase the efficiency and flow rate of an EHD pump, IEEE Trans. Ind. Appl. **26**, 42 (1990).
[46] M. Ashjaee and S. R. Mahmoudi, Experimental study of electrohydrodynamic pumping through conduction phenomenon using various fluids, *2005 Annual Report Conference on Electrical Insulation and Dielectric Phenomena* (IEEE, Nashville, 2005), pp. 495–498.
[47] M. Zhang, I. Lashgari, T. A. Zaki, and L. Brandt, Linear stability analysis of channel flow of viscoelastic Oldroyd-B and FENE-P fluids, J. Fluid Mech. **737**, 249 (2013).
[48] D.-L. Chen, K. Luo, J. Wu, and H.-L. Yi, Electrohydrodynamic conduction pumping of a viscoelastic dielectric fluid with the Onsager-Wien effect, Phys. Fluids **33**, 113101 (2021).
[49] F. Beunis, F. Strubbe, M. Marescaux, J. Beeckman, K. Neyts, and A. R. Verschueren, Dynamics of charge transport in planar devices, Phys. Rev. E **78**, 011502 (2008).
[50] G. Prilutski, R. Gupta, T. Sridhar, and M. Ryan, Model viscoelastic liquids, J. Non-Newtonian Fluid Mech. **12**, 233 (1983).
[51] W.-H. Cai, Y.-Y. Li, H.-N. Zhang, Y.-K. Li, J.-P. Cheng, X.-B. Li, and F.-C. Li, An efficient micro-mixer by elastic instabilities of viscoelastic fluids: Mixing performance and mechanistic analysis, Int. J. Heat Fluid Flow **74**, 130 (2018).
[52] M. Z. Bazant, Electrokinetics meets electrohydrodynamics, J. Fluid Mech. **782**, 1 (2015).
[53] F. Pimenta and M. Alves, Stabilization of an open-source finite-volume solver for viscoelastic fluid flows, J. Non-Newtonian Fluid Mech. **239**, 85 (2017).
[54] S. Xue and G. W. Barton, An unstructured finite volume method for viscoelastic flow simulations with highly truncated domains, J. Non-Newtonian Fluid Mech. **233**, 48 (2016).

[55] M. Yazdani and J. Seyed-Yagoobi, Numerical investigation of electrohydrodynamic-conduction pumping of liquid film in the presence of evaporation, J. Heat Transfer **131**, 135 (2009).
[56] J.-P. Cheng, H.-N. Zhang, W.-H. Cai, S.-N. Li, and F.-C. Li, Effect of polymer additives on heat transport and large-scale circulation in turbulent Rayleigh-Bénard convection, Phys. Rev. E **96**, 013111 (2017).
[57] B. Thomases and M. Shelley, Transition to Mixing and Oscillations in a Stokesian Viscoelastic Flow, Phys. Rev. Lett. **103**, 094501 (2009).
[58] A. Groisman and V. Steinberg, Elastic turbulence in curvilinear flows of polymer solutions, New J. Phys. **6**, 29 (2004).
[59] C. E. Wagner and G. H. McKinley, The importance of flow history in mixed shear and extensional flows, J. Non-Newtonian Fluid Mech. **233**, 133 (2016).
[60] B. Malraison and P. Atten, Chaotic Behavior of Instability Due to Unipolar Ion Injection in a Dielectric Liquid, Phys. Rev. Lett. **49**, 723 (1982).